

# Directed Chemical Evolution via Navigating Molecular Encoding Space

Lin Wang<sup>1</sup>, Yifan Wu<sup>2</sup>, Hao Luo<sup>3</sup>, Minglong Liang<sup>3</sup>, Yihang Zhou<sup>4</sup>, Cheng Chen<sup>3</sup>,  
Chris Liu<sup>3</sup>, Jun Zhang<sup>3</sup>, Yang Zhang<sup>1,2,4,5\*</sup>

<sup>1</sup>*Center for AI and Computational Biology, Institute of Systems Medicine, Chinese Academy of Medical Sciences, 215123, China*

<sup>2</sup>*Department of Computer Science, School of Computing, National University of Singapore, 117417, Singapore*

<sup>3</sup>*DeepMed Technology (Suzhou) Co., Ltd, 215123, China*

<sup>4</sup>*Cancer Science Institute of Singapore, National University of Singapore, 117599, Singapore*

<sup>5</sup>*Department of Biochemistry, Yong Loo Lin School of Medicine, National University of Singapore, 117596 Singapore*

\*Correspondence should be addressed to Yang Zhang, [zhang@nus.edu.sg](mailto:zhang@nus.edu.sg).

## Abstract

Deep-learning techniques have significantly advanced small-molecule drug discovery. However, a critical gap remains between representation learning and small molecule generations, limiting their effectiveness in developing new drugs. We introduce Ouroboros, a unified framework that integrates molecular representation learning with generative modeling, enabling efficient chemical space exploration using pre-trained molecular encodings. By reframing molecular generation as a process of encoding space compression and decompression, Ouroboros resolves the challenges associated with iterative molecular optimization and facilitates directed chemical evolution within the encoding space. Comprehensive experimental tests demonstrate that Ouroboros significantly outperforms conventional approaches across multiple drug discovery tasks, including ligand-based virtual screening, chemical property prediction, and multi-target inhibitor design and optimization. Unlike task-specific models in traditional approaches, Ouroboros leverages a unified framework to achieve superior performance across diverse applications. Ouroboros offers a novel and highly scalable protocol for rapid chemical space exploration, fostering a potential paradigm shift in AI-driven drug discovery.

## 40 **Introduction**

41 Artificial neural networks have shown remarkable ability to autonomously identify  
42 underlying data structures through their advanced representation learning capabilities<sup>1,2</sup>.  
43 Many techniques originally developed for natural language processing and image  
44 generation<sup>3–5</sup> have been successfully applied to drug discovery. For instance, considerable  
45 progress has been recently achieved in leveraging deep neural networks to learn  
46 interpretable molecular representations and encodings<sup>6</sup>, which can be of critical help in  
47 molecular property prediction and ligand-based virtual screening<sup>7–11</sup>.

48 Most recently, growing interests have been shown in generative AI for drug design. This  
49 approach often builds upon Quantitative Structure-Activity Relationship (QSAR), a  
50 technique originally developed 60 years ago<sup>12</sup> and now enhanced by molecular  
51 representation learning models to evaluate molecules produced by molecular generators<sup>13</sup>.  
52 While it helps facilitate iterative molecular generation, it limits models' capacity to  
53 perceive optimization directions. To partly address this, researchers have explored  
54 integrating drug property prediction and binding pocket condition into the training process  
55 of generative models<sup>14–18</sup>. However, this integration has posed considerable challenges in  
56 model extrapolation and reusability, mainly due to the inherent disconnections between  
57 molecular representation learning and molecular generation, a critical yet often overlooked  
58 gap that impedes the direct application of insights gained from representation learning into  
59 generative models.

60 Another emerging approach to molecular generation involves searching for neighbors  
61 of known drug molecules within the chemical space<sup>19</sup>. The effectiveness of the approach  
62 is highly correlated with the relationship between chemical space and encoding space  
63 learned by representation models. Although evidence suggests that chemical structures and  
64 neural network encodings may share common grounds, e.g., similar chemical structures  
65 often exhibit analogous biological activities, just as similar encodings yield comparable  
66 property outputs, a robust model for quantitatively mapping encoding to chemical space  
67 remains absent, hindering the effective application of the neighbor-search-based generative  
68 models in drug discovery.

69 To address these challenges, we introduce Ouroboros (as shown in **Figure 1a**), a new  
70 protocol to bridge the gap between representation learning and generative AI models and  
71 facilitate chemical space navigation for drug discovery. For doing this, Ouroboros first  
72 employs representation learning to encode molecular graphs into 1D vectors. These  
73 encodings are then independently decoded to predict both molecular properties and  
74 molecular structures, a process also known as chemical space decompression. One aim of  
75 Ouroboros is to transform the focus from traditional virtual screening<sup>9</sup>, which often relies  
76 on property predictors and encoding similarities for screening compound library, to  
77 directed chemical evolution within the encoding space to improve the effectiveness  
78 (**Figure S1**). Additionally, leveraging the encoding space for molecular structure  
79 decompression enables generative AI to integrate chemical knowledge from representation  
80 learning for guiding the directed chemical evolution of molecules. To examine the practical  
81 feasibility, we present a multi-level case study of the Ouroboros protocol, involving an  
82 independent representation learning for molecular encoder (**Figure 1b**), a molecular  
83 structure decoder to reconstruct the molecular encoding to molecular SMILES (**Figure 1c**),  
84 and a molecular property decoder to navigate the directed chemical evolution (**Figure 1d**).

85 Furthermore, we explore three distinct strategies for chemical evolution, offering insights  
86 into the practical applications of Ouroboros in drug discovery.  
87

## 88 **Results**

### 89 **Compressing the chemical space through similarity learning**

90 Representation learning creates a structured encoding space to interpret chemical  
91 molecular structures, with the assumption that molecules with similar chemical structures  
92 or pharmacological properties are positioned in proximity within encoding space. In a  
93 previous study, we demonstrated that incorporating Conformational Space Similarity (CSS)  
94 yields a generic molecular representation for ligand-based drug discovery<sup>9</sup>. To improve the  
95 performance of molecular representation learning, here we introduce two kinds of inter-  
96 molecular similarities, including an extended CSS with enhanced space searching and  
97 molecular fingerprint similarity (MFS) (see **Methods**). Furthermore, we propose a new  
98 similarity learning strategy that projects molecular encodings into multiple molecular  
99 similarities, aiming to enhance the capacity of the molecular encoder for generic and  
100 informative molecular encoding.

101 The pre-training architecture of representation learning in Ouroboros is outlined in  
102 **Figure S2**. The molecular encoder, which transforms molecular graphs into 1D encoding  
103 vectors, is pre-trained on a similarity matrix constructed from pairwise similarities between  
104 query and reference molecules. The 1D representations are then projected by two external  
105 projection heads into MFS and CSS respectively with the training process guided by the  
106 Mean Squared Error (MSE) loss. As shown in **Figure S3**, the Spearman correlation on the  
107 validation dataset reached convergence after about 20,000 pre-training steps and showed a  
108 similar performance on the test set (**Table S1**).

109 **Figure 1b** illustrates how the molecular encoding is extracted from molecule graphs,  
110 where atoms and chemical bonds in the molecular graphs are represented through a GNN  
111 for message passing. The resulting parameterized graph is then processed through a global  
112 attention pooling module<sup>20</sup> to construct the molecular encoding. The pre-trained encoder  
113 captures the varying contributions of different atoms to the overall molecular encoding.  
114 For atoms of the same element type but with distinct pharmacophore features, the  
115 Ouroboros encoder assigns differentiated weights. For example, a nitrogen atom with  
116 positive charge is weighted differently from those in amide groups (**Figure S4**). Moreover,  
117 the model demonstrates heightened attention to bulky hydrophobic groups when they  
118 appear, emphasizing their importance in pharmacophore and conformational flexibility.  
119

### 120 **Benchmarking the Ouroboros encoder for virtual screening and property prediction**

121 Directed chemical migration within the Ouroboros encoding space requires diverse  
122 property decoders to guide the optimization process, such as molecular similarity and  
123 molecular property predictors (**Figure S1**). Consequently, the generality and versatility of  
124 molecular encodings play a critical role in determining the capability of Ouroboros in drug  
125 discovery. Ideally, these encodings should be trained on a limited subset of molecular  
126 structures while maintaining the ability to generalize across large-scale benchmark datasets,  
127 such as 1,463,336 molecules in DUD-E<sup>21</sup> and 2,808,885 in LIT-PCBA<sup>22</sup>. Additionally, they  
128 should exhibit superior performance across various molecular property modeling tasks to  
129 ensure broad applicability and robustness.

130     **Ligand-based virtual screening.** To examine the potential of Ouroboros encoder for  
131 virtual screening, we estimate the chemical similarity of two molecules based on the cosine  
132 or Pearson similarity between 1D encoding vectors. **Figure 2a** compares it with 6 baseline  
133 methods using an early enrichment metric called Boltzmann-enhanced discrimination of  
134 receiver operating characteristic (BEDROC)<sup>23</sup> across two virtual screening benchmarks  
135 (DUD-E<sup>21</sup> and LIT-PCBA<sup>22</sup>). The results show that despite the relatively small training  
136 dataset, Ouroboros encoding achieves the highest enrichment scores in both benchmarks.  
137 Furthermore, as shown in **Table S2**, Ouroboros outperformed the baseline methods on most  
138 of other metrics, including AUPRC, AUROC, enrichment factor (EF), and log AUC. These  
139 results suggest that the Ouroboros encodings are more effective on clustering molecules  
140 with similar pharmacological features in proximity within the encoding space compared to  
141 the baseline methods, supporting the use of Ouroboros encoding similarity in directed  
142 chemical migration.

143     **Chemical property prediction.** The molecular property predictor in Ouroboros is  
144 implemented by mapping molecular encodings to properties via deep neural networks.  
145 **Figure 2b** presents the average Spearman correlation coefficient (SPEARMANR) of the  
146 Ouroboros predictor on 10 different molecular property datasets, which is significantly  
147 higher than that of AI-based GeminiMol and fingerprint-based CombineFP<sup>9</sup>. It also  
148 outperformed FP-GNN<sup>24</sup>, which was specifically designed for molecular property  
149 modeling by integrating multiple fingerprints with GNNs. If we check the individual  
150 properties, Ouroboros achieved the highest SPEARMANR in six out of 10 property tasks  
151 among all four predictors (**Table S3**). As an illustration, **Figure 2c** shows a head-to-head  
152 comparison of Ouroboros with CombineFP, where Ouroboros not only excels in relatively  
153 simple tasks, such as lipophilicity and hydration free energy prediction, but also achieves  
154 substantial improvements in more challenging tasks like steady-state volume of  
155 distribution and clearance rate. These results underscore the strong generalizability of  
156 Ouroboros encodings, which are crucial for training effective property predictors across a  
157 diverse range of downstream molecular property tasks.

158  
159 **Multi-target cancer inhibitor discovery using Ouroboros molecular encoder**

160     **Strategy for multi-target cancer inhibitor identification.** Similarity-based virtual  
161 screening is a widely used approach in ligand-based drug discovery, aiming to identify  
162 novel chemical scaffolds by retrieving new molecules that resemble known active  
163 compounds. Given the outstanding performance of Ouroboros in the DUD-E and LIT-  
164 PCBA benchmarks, we apply the encoder to a challenging multi-target drug discovery task  
165 to evaluate its practical utility. This task focuses on identifying multi-target inhibitors for  
166 five common cancer driver gene mutations, targeting synthetic lethality (for tumor  
167 suppressor genes) or promoting cell proliferation (for oncogenes).

168     A total of 10 distinct drug targets and 119 reference compounds are included in the  
169 experiment. Following the strategy outlined in **Figure 3a**, we enrich potential active  
170 molecules through similarity screening, followed by molecular docking to select candidate  
171 compounds for experimental assay. We anticipated that Ouroboros would identify  
172 structurally novel inhibitors from the Enamine REAL diversity set<sup>25</sup>, capable of  
173 simultaneously targeting at least two of these drug targets.

174     **Experimental validation.** A total of 18 molecules are successfully synthesized for  
175 enzyme activity assay, of which 7 compounds (38%) are active, and 3 compounds (16%)

176 exhibited multi-target inhibitory behavior as expected (**Table S4**). **Figure 3b** summarizes  
177 the results of the 3 identified hit molecules, each achieving a maximum similarity of over  
178 0.5 with the active reference molecules of three targets of interest, including PI3K $\alpha$ , the  
179 phosphatidylinositol 4,5-bisphosphate 3-kinase catalytic subunit alpha isoform; PI3K $\gamma$ , the  
180 phosphatidylinositol 4,5-bisphosphate 3-kinase catalytic subunit gamma isoform; and  
181 AURKA, the aurora kinase A, which demonstrates appreciable inhibitory activity in  
182 enzymatic assays.

183 Notably, compound #13 exhibited superior activity across all three targets, with an  $IC_{50}$   
184 in the nanomolar range for AURKA, highlighting its potential as a promising lead  
185 compound. However, the testing results of all 18 candidate compounds (**Table S4**)  
186 indicated that none showed an ability to inhibit more than four targets simultaneously. This  
187 limitation may be attributed to the relatively low throughput of the experiment and the use  
188 of only a 48.2M subset of the REAL library<sup>25</sup> during the screening. Additionally, the  
189 findings confirmed that compounds #2, #6, and #13 are not pan-kinase inhibitors, which  
190 selectively inhibit PI3K and AURKA. Overall, we identified three multi-target hit  
191 molecules from a 48.2M compound dataset by Ouroboros combined with molecular  
192 docking. These results show the application potential of Ouroboros encoding in similarity  
193 screening and further corroborate the ability of Ouroboros molecular encoding to  
194 generalize to ultra-large molecular structure datasets. This provides credibility to perform  
195 directed chemical evolution in this molecular encoding space.  
196

### 197 **Decompressing chemical structures from molecular encoding space**

198 Chemical language encoders and decoders are typically trained jointly to ensure the  
199 accurate reconstruction of molecular encodings from hidden layers. However, this coupling  
200 presents challenges for applying molecular representation learning in generative AI. One  
201 key issue is that the information embedded within the intermediate hidden layers of  
202 encoder-decoder models often fails to generalize effectively across diverse molecular  
203 properties. Furthermore, as shown in **Table S2**, chemical language models such as  
204 ChemBERTa<sup>26,27</sup>, do not demonstrate a substantial advantage over traditional molecular  
205 fingerprint-based methods in identifying structurally similar molecules with comparable  
206 biological activity. These findings indicate that molecular encodings derived from  
207 conventional chemical language pre-training strategies may be insufficiently optimized for  
208 capturing the chemical space relevant to drug discovery applications.

209 **More than 80% structures are rapidly recovered in validation.** In Ouroboros, we  
210 developed a new molecular structure decoder that reconstructs the original SMILES  
211 representations of molecules from their encoded 1D vectors using a Transformer-based  
212 architecture (**Figure S5**). As shown in **Figure S6**, the model converges rapidly within a  
213 single training epoch. To assess its performance, **Figure S7** presents the AtomPairs<sup>28</sup> MFS  
214 between the actual molecular structures and those reconstructed by the Ouroboros decoder  
215 in the validation set, where the mean similarity curve quickly stabilizes at an 80% threshold  
216 as batch numbers increase, demonstrating the efficiency and robustness of the Ouroboros  
217 decoder in molecular structure recovery from 1D encodings.

218 **Similarity declines more rapidly than validity upon perturbations.** To further assess  
219 the Ouroboros decoder's ability to explore latent molecular structures within the encoding  
220 space, we evaluate whether the model can generate valid and diverse molecular structures  
221 by introducing stochasticity into the decoding process. As shown in **Figure S8**, we

222 employed two approaches for randomized decoding: (1) perturbing molecular encoding  
223 vectors by adding noise based on the encoding space distribution and (2) introducing  
224 randomness into the token sampling process using the Gumbel-max technique<sup>29</sup>. As  
225 expected, the similarity between the original and decoded molecules decreases with  
226 increasing temperature and noise levels. However, the similarity curve declines more  
227 rapidly than the validity curve (which measures the proportion of decoded molecules with  
228 chemically reasonable valence bonds), indicating that Ouroboros effectively generates  
229 novel and diverse molecular structures while maintaining structural validity. These findings  
230 highlight again the effectiveness of the proposed molecular decoder framework in  
231 accurately reconstructing molecular structures from their 1D encodings.  
232

### 233 **Directed chemical evolution in encoding space for novel drug generation**

234 One primary objective of Ouroboros is to generate novel and chemically diverse  
235 molecular structures beyond the conventional scope of medicinal chemistry. To accomplish  
236 this, Ouroboros employs a directed chemical evolution approach, initiating the process with  
237 either Gaussian noise or a predefined molecule. The optimization is guided by a loss  
238 function constructed from molecular properties, refining the encoding vectors accordingly.  
239 By iteratively decoding molecules throughout the optimization, a progressive trajectory of  
240 molecular structure evolution emerges, facilitating the discovery of diverse and innovative  
241 scaffolds. The resulting molecules can then be selected for further experimental validation,  
242 guided by molecular docking, retrosynthetic analysis, and expert input from medicinal  
243 chemists (**Figure S9**).

244 **Chemical structure propagation.** To evaluate the effectiveness of directed chemical  
245 evolution, we first examine whether stochastic propagation can progressively modify the  
246 structure of the starting molecule and generate novel chemical scaffolds. Using aspirin as  
247 an illustrative example, **Figure 4a** demonstrates that the molecular structures generated  
248 through this process gradually diverge from the initial molecule while maintaining an  
249 observable similarity. Meanwhile, their encoding similarity decreases as propagation  
250 progresses. This finding suggests that exploring the neighboring regions of Ouroboros in  
251 the encoding space can uncover structural analogs of the starting molecule, supporting the  
252 use of Ouroboros for molecular generation.

253 **New drug design through directed migration.** The opposite of stochastic propagation  
254 is directed migration, a strategy that employs a loss function to guide the directed  
255 optimization of molecular encoding, thus permitting the directed optimization of chemical  
256 structures. As a demo, we examine directed molecular optimization guided by two specific  
257 properties: water solubility and membrane permeability. As shown in **Figure 4b**, starting  
258 from a hydrophobic molecule, Ouroboros successfully generates molecules with improved  
259 solubility while preserving overall structural similarity. Similarly, beginning with a highly  
260 flexible and strongly hydrophilic (led to poorly permeability) molecule, Ouroboros  
261 produced structures with reduced flexibility and carrying positive charges, which exhibited  
262 enhanced predicted membrane permeability. This result demonstrates that Ouroboros  
263 encoder is capable of selectively optimizing specific properties of the molecules during the  
264 migrations.

265 To further evaluate the model's generalizability, **Figures 4c** and **4d** present solubility  
266 and membrane permeability optimization results on a broader scale, featuring four  
267 representative organic molecules: two with low membrane permeability (Amoxicillin, an

268 antibiotic, and Diosmin, a natural product) and two hydrophobic molecules with poor water  
269 solubility (initial structures shown in **Figure S10**). The loss function was designed to  
270 simultaneously enhance solubility, membrane permeability, and lipophilicity, while  
271 maintaining structural similarity to the original molecules (as described in Methods).  
272 Despite applying the same loss function to both categories of molecules with suboptimal  
273 properties, Ouroboros' directed migration successfully generated multiple molecules with  
274 notable improvements in membrane permeability or solubility, while preserving an  
275 encoding similarity above 0.6. These findings underscore the versatility and effectiveness  
276 of Ouroboros' directed migration approach in molecular property optimization.

277 **Directed migration enhances docking scores of chemical compounds.** In **Figure S11**,  
278 Ouroboros is utilized to map a migration pathway between the encoding vectors of two  
279 inhibitors with distinct scaffolds ([1,3,5]-triazine derivative and 5-heterocycle pyrazolo  
280 pyridine), both targeting 3',5'-cyclic-AMP phosphodiesterase 4B (PDE4B), a crucial  
281 regulator of various physiological processes<sup>30</sup>. Docking the molecular decoys generated  
282 along this pathway into the PDE4B binding pocket revealed that the intermediates retained  
283 similar binding poses to the two reference molecules. Notably, three intermediate  
284 molecules along the migration trajectory exhibited superior docking scores compared to  
285 both reference compounds, highlighting Ouroboros' potential in scaffold hopping and  
286 structural optimization.

287  
288 **Dual-target drug optimization through decoding-based chemical fusion**  
289 The data in **Figure 3b** indicate that AURKA and PI3K $\gamma$  are kinase targets amenable  
290 for simultaneous inhibition. This finding motivated us to explore whether Ouroboros could  
291 integrate pharmacophore features from two sets of reference molecules to generate novel  
292 dual-target inhibitors. To investigate this, we conducted similarity screening on the  
293 Enamine REAL diversity set<sup>25</sup> (the training dataset for the molecular decoder) to identify  
294 potential dual-target inhibitors for AURKA and PI3K $\gamma$ . In parallel, the same reference  
295 compounds were input into Ouroboros for chemical fusion, enabling a direct comparison  
296 between the candidate compounds generated by both approaches (**Figure 5a**).

297 **Dual-target molecules are scarce in reference molecules.** Analysis of the encoded  
298 similarity matrix for the two reference sets revealed a maximum similarity of 0.61 between  
299 them (**Figure 5b**). However, none of these compounds exhibited dual-target inhibition,  
300 suggesting that molecules with higher similarity to both reference sets might be needed to  
301 improve success rates. To address this, we retained partially fused molecules from the  
302 chemical fusion process that achieved a maximum similarity exceeding 0.65 for both  
303 targets. Among these, the top 500 molecules (ranked by synthetic accessibility) were  
304 selected and compared directly with the top 500 molecules from similarity screening in a  
305 head-to-head evaluation.

306 **Chemical fusion helps design dual-target molecules.** As shown in **Figure 5c**,  
307 molecules generated through chemical fusion exhibited significantly higher encoded  
308 similarity, with many achieving similarity scores above 0.7 for both targets. To further  
309 assess the development potential of these candidate compounds, we performed molecular  
310 docking to evaluate their binding affinity and calculated MM-GBSA (Molecular  
311 Mechanics Generalized Born Surface Area) binding free energy. The results demonstrated  
312 that chemical fusion produced more compounds with superior docking scores and binding  
313 free energies for both targets.

314     Additionally, we compared the ligand efficiency of both groups (removing the effect of  
315     ligand size), further confirming Ouroboros' advantage in identifying highly efficient dual-  
316     target inhibitors. Overall, chemical fusion has the superior capability of lead compound  
317     screening over similarity screening, while this capability is expected to further improve as  
318     scaling up of the training dataset for molecular decoder.  
319

## 320     Discussion

321     Representation learning and generative AI have gained significant attention in drug  
322     discovery, yet a fundamental disconnect between these domains has limited the effective  
323     use of chemically meaningful representations for molecular design. To bridge this gap, we  
324     introduce Ouroboros, a novel framework that seamlessly integrates molecular  
325     representation learning with generative AI through three key components: (1) a generalized  
326     molecular encoder that projects chemical structures into 1D encoding vectors, (2) an  
327     independent structural decoder that reconstructs SMILES sequences, and (3) a chemical  
328     space navigator that enables directed molecular optimization. Notably, the decoupled  
329     training paradigm allows Ouroboros to acquire chemically relevant knowledge without  
330     generation constraints during pretraining, achieving superior performance in similarity-  
331     based virtual screening and molecular property prediction.

332     Ouroboros incorporates a similarity learning strategy that significantly enhances data  
333     efficiency, enabling effective pretraining on a compact chemical dataset (<150,000  
334     molecules) while demonstrating exceptional virtual screening performance on large-scale  
335     benchmarks such as DUD-E and LIT-PCBA (>1 million molecules). Its real-world utility  
336     was further validated through multi-target drug discovery, successfully identifying three  
337     novel multi-target inhibitors from a 48.2 million-compound diversity library, showcasing  
338     its strong generalization across chemical spaces.

339     Architecturally, Ouroboros employs an auto-regressive Transformer decoder that  
340     reconstructs SMILES sequences from compressed 1D encodings, enabling two generative  
341     strategies: directed migration and chemical fusion. Benchmark evaluations on molecular  
342     property optimization and dual-target inhibitor design confirm its superior performance  
343     over existing methods. In this context, Ouroboros effectively bridges the gap between  
344     molecular representation learning and generative AI, establishing a new paradigm for  
345     continuous chemical evolution in encoding space. Beyond these strategies, Ouroboros can  
346     also integrate other AI-driven models, leveraging them as loss functions to optimize  
347     molecular properties.

348     While Ouroboros has shown superior performance in predicting multiple molecular  
349     properties, the current benchmark includes only 10 molecular properties, indicating  
350     significant opportunities for future development. Moreover, there is increasing interest in  
351     generating molecules with strong binding affinity for specific biological targets. Currently,  
352     Ouroboros does not predict drug-target binding affinity directly. Instead, it relies on  
353     molecular docking to identify molecules along the transition path with superior docking  
354     scores and binding poses. This suggests a keen need to incorporate protein representations  
355     into the training of drug-target binding affinity prediction models to further enhance the  
356     capabilities of the Ouroboros framework. With continuous progress in molecular  
357     representation learning, we anticipate that Ouroboros, supported by ongoing community-  
358     driven innovations, will evolve into a pivotal tool for AI-powered drug discovery. Its

359 potential to streamline early-stage drug development and molecular structure optimization  
360 offers promising avenues for advancing pharmaceutical research.  
361

## 362 Methods

363 The Ouroboros protocol designs for unified drug molecule representation and  
364 generation and employs three independent modules: (1) a molecular encoder that  
365 compresses molecular structures into 1D vectors; (2) a property decoder that translates 1D  
366 vectors into molecular properties; and (3) a structural decoder that reconstructs molecular  
367 structures from 1D vectors (**Figure 1**). The protocol is flexible and can be easily extended  
368 to integrating other representation learning models with domain-specific knowledge for  
369 molecular encoding.  
370

### 371 AI model architecture

372 **Representation and message passing of molecular graph.** To compress the chemical  
373 space, a molecular encoder of 1D molecular encoding with a size of 2048 is pre-trained by  
374 molecular similarity learning, which promotes the model to identify molecules with similar  
375 chemical structures and pharmacophore features. For this, we first converts SMILES  
376 representations into molecular graphs, which are then processed by a GNN-based  
377 Weisfeiler-Lehman Network (WLN)<sup>31</sup> for features updating (**Figure S12a**). Next, a global  
378 self-attention pooling module is applied to compute atom-wise attention weights. These  
379 weights are finally used to aggregate atomic features into a molecule-level encoding vector,  
380 which can be further utilized for various pre-training tasks, including MFS and CSS.

381 The small molecular structure in encoder is represented as a graph  $G = (V, E)$ , with  $V$   
382 representing atoms and  $E$  chemical bonds. The atom features include atom type,  
383 hybridization, formal charge, chiral tag, whether the atom is in a ring, and whether the atom  
384 is aromatic. The bond features include whether or not they are conjugated, ring-forming,  
385 and chiral types. Both the construction of molecular graphs and the message passing are  
386 implemented through the DGL<sup>32,33</sup> package.

387 As shown in **Figure S12a**, the GNN processes molecular graphs by iteratively updating  
388 atom and bond features through a message-passing scheme. The input atom features  $\mathbf{h}_v^{(0)}$   
389 are projected into a higher-dimensional space using a linear transformation followed by a  
390 ReLU<sup>34</sup> activation:

$$391 \quad \mathbf{h}_v^{(0)} = \text{ReLU}(\mathbf{W}_{in}\mathbf{h}_v + \mathbf{b}_{in}) \quad (1)$$

392 where  $\mathbf{W}_{in}$  is the learnable weight matrix, and  $\mathbf{b}_{in}$  is the bias term. For each bond feature  
393  $\mathbf{e}_{uv}$  contacting atoms  $u$  and  $v$ , a message is generated by concatenating the source atom  
394 features  $\mathbf{h}_u$  and  $\mathbf{e}_{uv}$ :

$$395 \quad \mathbf{m}_{uv} = \text{ReLU}(\mathbf{W}_{contact}[\mathbf{h}_u \parallel \mathbf{e}_{uv}] + \mathbf{b}_{contact}) \quad (2)$$

396 where  $\parallel$  denotes concatenation. These messages are used to update the bonds features:

$$397 \quad \mathbf{e}_{new}^{uv} = \mathbf{m}_{uv} \quad (3)$$

398 The atom features are updated by aggregating messages from neighboring bonds and  
399 combining them with the atom's previous features:

400 
$$\mathbf{h}_v^{(t+1)} = \text{ReLU} \left( \mathbf{W}_{aggregate} \left[ \mathbf{h}_v^{(t)} \parallel \sum_{u \in \mathcal{N}(v)} \mathbf{e}_{uv}^{new} \right] + \mathbf{b}_{aggregate} \right) \quad (4)$$

401 where  $\mathcal{N}(v)$  is the set of neighbors of atom  $v$ , the  $t$  represents the times of massage  
 402 passing (4 times in this work). Then, atom features  $\mathbf{h}_v$  and bond features  $\mathbf{e}_{uv}$  are  
 403 independently projected into a latent space to prepare them for further interactions,  
 404 element-wise multiplicated, and aggregated from all neighbors of the atom  $v$ :

405 
$$\mathbf{h}_v^{final} = \mathbf{W}_{self} \mathbf{h}_v \odot \left( \sum_{u \in \mathcal{N}(v)} (\mathbf{W}_{bond} \mathbf{e}_{uv} \odot \mathbf{W}_{atom} \mathbf{h}_{uv}) \right) \quad (5)$$

406 The final atom representation combines the aggregated neighbor features and a self-  
 407 loop attention through element-wise multiplication.

408 **Global attention pooling module.** The model implements global self-attention pooling  
 409 through the following steps: for each atomic features  $\mathbf{h}_i$  in the molecular graph, a MLP  
 410 predicts its attention weight, denoted as  $a_i$ . These weights are normalized using the  
 411 SoftMax function to ensure they sum to 1:

412 
$$w_i = \frac{\exp(a_i)}{\sum_i \exp(a_i)} \quad (6)$$

413 Each atomic feature is then scaled by its normalized attention weight, and the scaled  
 414 features are summed to generate the graph-level encoding  $\mathbf{H}_{graph}$ :

415 
$$\mathbf{H}_{graph} = \sum_{\{i \in V\}} \mathbf{h}_i w_i \quad (7)$$

416 As shown in **Figure S12b**, the MLP begins by projecting the atom features from 2048  
 417 to 6144 dimensions, followed by reductions to 1024 and 128 dimensions in sequence. The  
 418 linear projection in 128 dimensions is repeated three times before projecting the features  
 419 to a single dimension. Batch normalization is applied after the first two linear layers, and a  
 420 sigmoid activation function is applied after every linear layer, including the final layer  
 421 generating the 1-dimensional attention weight.

422 **Properties Decoder module for property modeling.** The property predictor in  
 423 Ouroboros consists of three neural network components (**Figure S12c**). The first  
 424 component includes a dropout layer (dropout rate: 0.5) that projects the molecular encoding  
 425 from 2,048 dimensions to 8,192 dimensions, followed by a sigmoid activation function.  
 426 The second component concatenates the molecular encoding generated by the first  
 427 component with the original molecular encoding, resulting in a 10,240-dimensional vector.  
 428 This vector is processed through two linear layers while maintaining the feature dimension  
 429 at 10,240, with LeakyReLU<sup>35</sup> activation and batch normalization applied between the  
 430 layers. The third component performs an element-wise addition of the input and output  
 431 features from the second component. The resulting features are processed through a linear  
 432 layer, batch normalization, and SiLU<sup>36,37</sup> activation, then projected to 1,024 dimensions.  
 433 This is followed by another round of batch normalization and SiLU<sup>36,37</sup> activation. Finally,  
 434 the features pass through one more linear layer with SiLU<sup>36,37</sup> activation to project them to

435 the dimensionality of the target property (1-dimensional for all properties in the  
436 benchmark).

437 **Representation of chemical language.** The tokenizer used in Ouroboros molecular  
438 decoder is a Byte-Pair<sup>38</sup> tokenizer, in which vocabularies were obtained by segmenting the  
439 SMILES of the compounds in our dataset. These tokenizers all include at least the basic  
440 elements that make up a pharmaceutical small molecule, such as C, N, O, S, P, c, n, o, s, F,  
441 Cl, Br, I, basic chemical bonds and isomer labels, such as, "=", "@", "/", "\",, and "#", as  
442 well as other special symbols, such as brackets and numbers.

443 **Molecular structural decoder module for encoding decompressor.** The main role of  
444 the structural decoder module is to transform 1D encoding vectors into probability  
445 distributions with specific length tokens. It is implemented by a Transformer decoder, and  
446 the 1D encoding vector serves as the input memory. Using an autoregressive generation  
447 strategy, the decoder predicts the next token in the SMILES sequence until the end token  
448 occurred. We train a 4-layer, 32-head Transformer decoder, equipped with layer  
449 normalization and SiLU<sup>36,37</sup> activation functions, to reconstruct the SMILES representation  
450 of molecular encodings by using the molecular encodings as memory tensors. For the target  
451 SMILES, rotational position encoding and an embedding layer are utilized to generate  
452 target tensors, which are used for teaching-force<sup>39</sup>.

453 A deep neural network projects hidden states onto the token vocabulary during each  
454 prediction step (**Figure S12d**). For the output features of the Transformer decoder, a 3-  
455 layer MLP is employed to project these features to match the number of tokens. Specifically,  
456 the hidden features are first transformed to 4096 dimensions, subsequently reduced to 1024  
457 dimensions, and finally mapped to logits over 43 distinct tokens.  
458

#### 459 **Data collection and training scheme**

460 **Molecular datasets.** We employed two molecular datasets of differing sizes to train and  
461 test the Ouroboros compressor and decompressor for molecular chemical space  
462 representation. The first dataset contains 126,248 distinct molecules, collected from five  
463 categories of resources: 1) The diverse molecular dataset previously utilized in  
464 GeminiMol<sup>9</sup>; 2) A macrocyclic peptide dataset CycPeptMPDB<sup>40</sup>; 3) The diverse molecular  
465 dataset in the Cell Painting Gallery<sup>41,42</sup>; 4) Molecules from the Protein Data Bank (PDB)<sup>43</sup>;  
466 5) A manual-collected dataset of common biological cofactors, polypeptides, and  
467 oligonucleotides. Out of the 126,248 query molecules, 4728, 32 and 64 reference molecules  
468 are randomly selected and paired with the query molecules to form three similarity matrices  
469 of 4728×126248, 32×126248, and 64×126248, which are used as training, validation and  
470 test datasets, respectively, for the Ouroboros compression encoder. When splitting the  
471 molecule datasets, we used a Tanimoto similarity cutoff of ECFP4 < 0.3 to ensure that the  
472 molecules in the validation and test sets are non-homologous to the training set.

473 The second dataset is a combination of the 48.2 M Enamine REAL Diversity set<sup>25</sup> and  
474 the core dataset of the 126,248 molecules, which are designed for the Ouroboros molecular  
475 decoding decompressor development. Here, the validation set comprised 200 molecular  
476 structures from the REAL dataset, 256 structures from the first four subsets in core  
477 molecular dataset, and 35 molecules in the 5<sup>th</sup> subset, while all remaining molecular  
478 structures were used for training.

479 **Molecular similarity matrices.** We designed two types of inter-molecular similarity  
480 scores, CSS and MFS, for molecular similarity learning. All molecules in the core

481 molecular dataset (126,248) are preprocessed, with calculations including the predictions  
482 of protonation under pH = 6.9 and tautomeric states by the LigPrep module<sup>44</sup> in the  
483 Schrödinger software package. For each molecule, the protonated and tautomeric state with  
484 the lowest penalty score was selected.

485 For a given pair of molecules, the CSS is determined by identifying the conformations  
486 with the highest pharmacophore similarity when superimposing all conformations of one  
487 molecule onto those of the other. In our previous work on GeminiMol<sup>9</sup>, we implemented a  
488 simplified version of CSS descriptors, where conformational space exploration was  
489 constrained using two energy window scaling factors (0.5060 and 1.4806 kcal/mol). To  
490 generate pseudo-labels for data augmentation, we preserved the minimum similarity during  
491 similarity calculation, which was used to estimate the conformational flexibility. While this  
492 pseudo-labeling approach lacks a clear physical interpretation, the application of CSS  
493 descriptors led to improved model performance, suggesting that a more refined CSS  
494 descriptor could further enhance model accuracy.

495 In Ouroboros, we employ a more detailed conformational search and CSS calculation  
496 approach by incorporating four energy windows, which are defined by multiplying the  
497 number of rotatable bonds with scaling factors of 0.5060, 0.14806, 0.88836, and 1.4806  
498 kcal/mol. Superimposition and similarity calculations are performed using PhaseShape<sup>45</sup>,  
499 where molecules are represented in pharmacophore space. Conformational searching is  
500 carried out using the Monte Carlo Multiple Minima (MCMM)<sup>46</sup> algorithm from the  
501 MacroModel module<sup>47,48</sup> within the Schrödinger software package, executing 10,000 steps  
502 under the OPLS4 force field<sup>49</sup>, with redundant conformations removed based on a 0.5 Å  
503 RMSD cutoff. During data augmentation, numerical calculations were streamlined by  
504 retaining only the difference between CSS values at the maximum and minimum energy  
505 windows. This strategy effectively captures molecular flexibility trends as a function of  
506 energy variations. Compared to GeminiMol<sup>9</sup>, the enhanced conformational search with  
507 additional energy windows, lower RMSD thresholds, and an optimized search process, is  
508 expected to improve the CSS calculation accuracy and physical interpretability without  
509 requiring complex data manipulations.

510 To construct the MFS matrix, three descriptors (ECFP4<sup>50</sup>, MACCS<sup>51</sup>, and AtomPairs<sup>28</sup>)  
511 are computed for each of the molecule pairs. For ECFP4<sup>50</sup> and MACCS<sup>51</sup>, we employed  
512 the Tanimoto similarity measure, while for AtomPairs<sup>28</sup>, the Tversky similarity measure  
513 was chosen, as it demonstrated superior virtual screening performance in prior evaluations<sup>9</sup>.  
514 To augment the data, the difference in similarity under the largest and smallest energy  
515 windows was computed and added to the similarity vectors.

516 Consequently, the final similarity representation for each molecule pair contains five  
517 CSS and three MFS descriptors.

518 **Similarity learning for molecular representation pre-training.** The projection head of  
519 Ouroboros was designed to project the learned molecular encoding into meaningful inter-  
520 molecular similarities (**Figures S2b-c**). The projection network consists of a series of fully  
521 connected layers with non-linear activation functions and normalization. Two encoding  
522 vectors of query and reference molecules were input to the two projection heads of MFS  
523 and CSS. The encoding vector first passes through a rectifier component, which expands  
524 the features to 5 times the dimension of the original encoding vector, passes the  
525 LeakyReLU<sup>35</sup> activation function and a batch normalization layer. Subsequently, the  
526 expanded features are concatenated with the original encoding vector and progressively

527 passed through linear layers, sequentially reducing dimensions from 24,576 to 2,048,  
528 followed by batch normalization. This process continues with a reduction from 2,048 to  
529 512 dimensions, another batch normalization step, and is repeated three times before being  
530 projected to the final output dimensions. The SiLU<sup>36,37</sup> activation function was added  
531 between all linear layers in the projection head. Finally, it outputs a value that was reset to  
532 the range of 0-1 through a sigmoid neuron in the projection head.

533 In the pre-training task of similarity learning, we train the Ouroboros encoder by  
534 continuously sampling data from the similarity matrix ( $126,512 \times 4,728$  in training set). In  
535 each batch, there are 512 query and 48 reference molecules, with 8 different similarity  
536 labels for each pair of molecules. The model is thus trained to predict a third-order matrix  
537 ( $512 \times 48 \times 8$ ), with the loss function being MSE between predicted and actual similarity  
538 scores.

539 During the similarity learning stage, training is performed using the AdamW<sup>52</sup> optimizer  
540 in PyTorch<sup>53</sup>, with a learning rate of  $5.0 \times 10^{-5}$  and a weight decay of 0.01. Two learning  
541 rate adjustment strategies are applied: (1) gradual increase at the beginning of training, and  
542 (2) cosine learning rate scheduling, which dynamically adjusts the learning rate based on  
543 training progress to prevent convergence to local optima. In the Ouroboros encoder, the  
544 WLN parameters are inherited from the GeminiMol model and remain frozen for the first  
545 2,000 training steps. The learning rate warmup starts at 10% of the original learning rate  
546 and increases linearly to the full learning rate over 10,000 steps. The minimum learning  
547 rate in the cosine learning rate schedule is set to 50% of the original learning rate, with a  
548 scheduling period of 10,000 steps. Additionally, an early stopping strategy is employed,  
549 where validation set performance is monitored every 200 steps. If no improvement is  
550 observed over 60 validation iterations, training is terminated early to prevent unnecessary  
551 computation.

552 **Molecular Property Modeling.** The training, validation, and test sets for the molecular  
553 property predictor are divided according to molecular scaffolds, ensuring that  
554 approximately 20% of the molecules in the test set possess novel scaffolds not present in  
555 the training set. During the training stage, MSE loss function and AdamW<sup>52</sup> optimizer with  
556 a learning rate of  $5.0 \times 10^{-5}$  was used in training. The batch size is determined by the size  
557 of the training dataset: a batch size of 96 is used for training sets exceeding 5000 samples,  
558 64 for those with more than 1000 samples but fewer than 5000, and 48 for training sets  
559 with fewer than 1000 samples. The learning rate scheduling strategy employed during  
560 training is identical to that used in pre-training; specifically, the period of learning rate  
561 schedule is set to 2000 steps for training sets larger than 5000 and 1000 steps for smaller  
562 training sets. Model performance is validated every 200 steps, and training is early stop if  
563 no performance improvement is observed over 60 cumulative validation evaluations.

564 **Training scheme for molecular structural decoder.** In the training of the molecular  
565 decoder, causal masking is applied to implement teaching-forcing<sup>39</sup>. To align its shape with  
566 the output tensor and integrate positional information, the teacher tensor is passed through  
567 an embedding layer followed by rotary positional encoding<sup>54,55</sup>. The training process uses  
568 the previously described learning rate scheduling strategy, with a period of 4000 steps. The  
569 AdamW<sup>52</sup> optimizer is employed with a learning rate of  $5.0 \times 10^{-5}$  and a weight decay  
570 of 0.01.

571 The training loss for the molecular structure decoder is computed using a weighted  
572 cross-entropy loss. The start-of-sequence token is excluded from the loss calculation. For

573 each token  $t_i$ , its weight is computed as inversely proportional to its frequency  $f_i$  in the  
574 batch relative to the total token count, capped at 100, i.e.,

575 
$$w_i = \min\left(\frac{N_{total}}{f_i}, 100\right) \quad (8)$$

576 where  $N_{total}$  is the total token count in the batch. If  $f_i = 0$ ,  $w_i$  is reset to 1. Padding tokens,  
577 indexed as 0 in the vocabulary, are ignored during loss computation. The token-wise cross-  
578 entropy loss (excluding padding tokens) matrix  $\mathcal{L}_{\text{CrossEntropy}}$  is multiplied elementwise by  
579 the weight matrix  $W$ :

580 
$$\mathcal{L}_{\text{tokens}} = \mathcal{L}_{\text{CrossEntropy}} \odot W \quad (9)$$

581 The final loss is obtained by averaging over all tokens ( $j$  is ground-truth token):

582 
$$\mathcal{L}_{\text{final}} = \frac{\sum_{i,j} \mathcal{L}_{\text{tokens}}[i,j]}{|\mathcal{T}_{\text{valid}}|} \quad (10)$$

583 where  $|\mathcal{T}_{\text{valid}}|$  is the number of valid tokens (excluding start-of-sequence token).

584

### 585 Downstream tasks for three independent modules

586 **Virtual screening.** In this study, we assessed the generalization capabilities of molecular  
587 encoders using the DUD-E<sup>21</sup> and LIT-PCBA<sup>22</sup> virtual screening benchmarks. In the  
588 benchmark tests of LIT-PCBA<sup>22</sup>, there are multiple active compounds for each target that  
589 can serve as reference molecules. Traditional baseline methods included ECFP4<sup>50</sup>,  
590 MACCS<sup>51</sup>, AtomPairs<sup>28</sup>, and Phase Shape<sup>45</sup>, while GeminiMol served as the AI-based  
591 baseline due to its use of a similar training strategy. For GeminiMol<sup>9</sup>, the Pearson  
592 correlation coefficient, as described in its original study, was used as the similarity metric.  
593 In the case of Ouroboros and ChemBERTa, cosine similarity was applied due to its  
594 computational simplicity, but performance comparable to the Pearson correlation  
595 coefficient. In this study, we use three different versions of ChemBERTa<sup>26,27</sup>, including the  
596 base model pre-trained on 100K SIMLES, and the two models Masked Language Modeling  
597 (MLM) and Multi-Task Regression (MTR) pre-trained on 77M SIMLES in ChemBERTa-  
598 2<sup>26,27</sup>, respectively. When using ChemBERTa to extract molecular coding, the batch size is  
599 set to 1 to avoid the effects of padding. Since the data for ChemBERTa comes from the  
600 PubChem dataset, which is the same source as the data for LIT-PCBA, we expect it to  
601 perform better.

602 For each query molecule  $q$ , we calculate the similarity to all reference molecules  $R$  and  
603 select the highest similarity value as the final score, i.e.,

604 
$$\text{sim}(q) = \max_{\{r \in R\}} (\text{sim}(r, q)) \quad (11)$$

605 In this work, the BEDROC was used in the virtual screening as the evaluation metric,  
606 where the  $\alpha$  of BEDROC was set to 160.9, corresponding to EF<sub>1%</sub><sup>23</sup>.

607 **Molecule property prediction.** To further evaluate molecular property modeling  
608 performance, we tested various models on ten diverse drug property datasets from TDC<sup>56</sup>.  
609 In this study, training, validation, and test sets were split based on molecular scaffolds,  
610 following the default data partitioning settings of TDC<sup>56</sup>, with 20% of the data reserved for  
611 the test set. Both Ouroboros and GeminiMol<sup>9</sup> use frozen molecular encoders, where fixed  
612 molecular encodings are directly projected onto molecular properties. CombineFP

613 extracted 2048-dimensional molecular fingerprints, including ECFP4<sup>50</sup>, FCFP6<sup>50</sup>,  
614 AtomPairs<sup>28</sup>, and TopologicalTorsion<sup>57</sup>, using RDKit<sup>58</sup>. These fingerprints are then  
615 analyzed by AutoGluon<sup>59</sup>, which automated the selection of optimal machine learning  
616 algorithms from methods such as neural networks, LightGBM<sup>60</sup>, and CatBoost<sup>61</sup>. FP-  
617 GNN<sup>24</sup> was tested with its default parameters and evaluated using the same data splits as  
618 the other approaches.

619 **Molecular structure generation.** For the structure decoder, we reconstructed molecular  
620 structures from 1D vectors in the validation set and evaluated their validity and similarity  
621 to the original molecules. For this task, the molecular datasets selected were from first four  
622 subsets of the core molecular dataset. These experiments assessed whether the model could  
623 maintain molecular validity while producing structural diversity.

624 We examined the model's ability to generate diverse molecular structures by introducing  
625 1) random Gaussian noise into 50% of the positions in the molecular encodings and 2)  
626 increasing the temperature of the autoregressive decoding process by Gumbel-max<sup>29</sup>  
627 technique. This method incorporates stochasticity into the decoding process while  
628 respecting the probability distribution determined by the model.

629 For the first validation approach, we used Gaussian noise and scaled by  $N \in$   
630  $[0.001, 0.0025, 0.005, 0.0075]$ . The perturbed encoding vector  $\mathbf{v}$  can be represented as:

$$631 \quad \mathbf{v} = \mathbf{E} + N \cdot (\mathbf{n} \odot \mathbf{m}) \quad (12)$$

632 where  $\mathbf{n} \sim \mathbf{N}(-1, 1)$ , and for each position  $i$  of  $\mathbf{E}$ , the mask  $m_i$  is defined as:

$$633 \quad m_i = \begin{cases} 1, & \text{with probability 0.5} \\ 0, & \text{otherwise} \end{cases} \quad (13)$$

634 For the second approach, we used the temperatures  $T \in [0.01, 0.1, 0.5, 1.0, 1.5, 2.0]$ . To  
635 sample token indices from a predicted probability distribution, we first apply the SoftMax  
636 function with a temperature  $T > 0$  to smooth or sharpen the distribution. The temperature-  
637 scaled log probabilities are computed as:

$$638 \quad \log \mathbf{p} = \log \text{SoftMax}\left(\frac{\mathbf{y}}{T}\right) \quad (14)$$

639 where  $\mathbf{y}$  is the predicted logits, and  $\mathbf{p}$  represents the normalized probabilities.

640 To enable sampling, we add Gumbel noise to the log probabilities. The Gumbel noise  
641  $\mathbf{g}$  is generated as:

$$642 \quad \mathbf{g} = -\log(-\log(\mathbf{u} + \epsilon)) \quad (15)$$

643 where  $\mathbf{u} \sim \mathbf{Uniform}(0, 1)$  and  $\epsilon$  is a small positive constant to avoid numerical instability.  
644 The noisy log probabilities  $\mathbf{s}$  are given by:

$$645 \quad \mathbf{s} = \log \mathbf{p} + \mathbf{g} \quad (16)$$

646 The sampled indices are obtained by taking the argmax over the  $\mathbf{s}$ .

647

#### 648 Applying the Ouroboros encoding in practical drug discovery

649 **Biological hypothesis and reference molecules.** In this study, a total of 5 cancer drivers  
650 are selected for multi-target drug screening. For KRAS, apart from itself, PI3K $\alpha$ , PI3K $\gamma$ ,  
651 MEK1/2, and PLK1 are selected as relevant targets. For TP53, synthetic lethal targets,  
652 WEE1 and CHK1/2, are selected. For SMAD4, AURKA is selected as a synthetic lethal

653 target. For CDKN2A/MTAP, PRMT5 is selected as a synthetic lethal target. For BRCA1/2,  
654 PARP1/2 is selected as the synthetic lethal target. We retrieve all molecules from ChEMBL  
655 with pChEMBL values greater than 7.0 for the relevant targets. These compounds are then  
656 clustered using AtomPairs fingerprints and visually inspected to ensure structural diversity.  
657 Ultimately, 119 compounds are selected as reference molecules.

658 **Similarity screening using Ouroboros encoding.** In similarity screening, cosine  
659 similarity is used as the calculation metric, retaining only the maximum similarity for each  
660 reference molecule within a target set, as described in Eq. (11). For query molecules with  
661 a similarity score below 0.5, the similarity value is reset to 0. Finally, the top 0.1% of  
662 molecules, ranked by the sum of similarities, are selected for subsequent molecular docking  
663 validation.

664 **Docking validation.** Although Ouroboros demonstrated superior early enrichment rates  
665 in benchmark tests, however, selection of a small number of optimal candidates by careful  
666 docking inspection is necessary due to the high cost of chemical synthesis. We further  
667 enriched potential active molecules using a hierarchical virtual screening process called  
668 GVSrun (<https://github.com/Wang-Lin-boop/CADD-Scripts/blob/main/GVSrun>) in which  
669 the docking program is Glide<sup>62</sup>. The resulting docking poses were visually inspected to  
670 exclude irrational structures, which mainly include unsaturated hydrogen bond donors,  
671 ligand strain energies, and solvent effects.

672 **Enzyme inhibitory assay.** A total of 18 compounds are successfully synthesized and  
673 subjected to enzymatic activity assays. The selected kinases for single-dose enzymatic  
674 screening (10 μM) include PIK3CA, PIK3CG, AURKA, MEK1, CHK1, PLK1, and WEE1,  
675 while PIK3CA, PIK3CG, and AURKA are further assessed for IC<sub>50</sub> determination. The  
676 enzymatic activity assay is conducted in a 384-well plate (Greiner, 784075) at 25°C for 60  
677 minutes. Each well contains 1 μM substrate, 1 nM kinase, and 4 μM ATP in assay buffer.  
678 After the reaction, 10 μL of kinase detection reagent is added to each well, followed by  
679 incubation at 25°C, centrifugation at 1,000 rpm for 1 minute, and a final incubation at 25°C  
680 for 1 hour. Fluorescence signals are measured at 620 nm (Cryptate) and 665 nm (XL665)  
681 using a BMG plate reader. IC<sub>50</sub> values are determined by nonlinear regression (curve fitting)  
682 using a variable slope (four-parameter model) in GraphPad Prism (v.8.0).

#### 683 **Implementation of directed chemical evolution**

684 **Stochastic Propagation.** By incrementally introducing noise to the encoding vector of  
685 the initial molecule, the progressive evolution of molecular structures can be observed. In  
686 the stochastic propagation experiment, we generate new molecular structures by adding  
687 random noise to the coding vector (**Figure S13a**).

688 For the entire encoding vector  $\mathbf{E}$ , we generate a standard Gaussian noise  $\mathbf{n} \sim \mathbf{N}(-1, 1)$ ,  
689 which was scaled by the standard deviation at each location, denoted as  $\sigma$ . The noise is  
690 further scaled to 0.05 and masked randomly at 50% of the locations. The perturbed  
691 encoding vector  $\mathbf{v}$  is represented as:

$$693 \quad \mathbf{v} = \mathbf{E} + 0.05 \cdot (\mathbf{n} \odot \sigma \odot \mathbf{m}) \quad (17)$$

694 where the mask  $\mathbf{m}$  is defined same as previous Eq. (13).

695 The propagation undergoes a total of 200 steps, with the molecular structure at each step  
696 generated using a molecular structure decoder operating at a temperature of 0.30. As the

697 number of steps increases, newly generated structures are incrementally accumulated,  
698 enabling thorough exploration of the local encoding space.

699 **Directed Migration.** Molecular encoding vectors can be optimized using techniques  
700 similar to training neural networks, where the encoding is directionally adjusted to optimize  
701 molecular properties as defined by the loss function. Starting from the initial molecular  
702 encoding vector, the optimization is performed using the AdamW<sup>52</sup> optimizer with a  
703 learning rate of  $2.0 \times 10^{-5}$  for 600 steps. After each step, the encoding vector is converted  
704 into a molecular structure using a molecular structure decoder with a temperature of 0.4  
705 (**Figure S13b**).

706 The loss function consists of two terms. The first term minimizes the absolute difference  
707 between the  $Sim_{start}$  and a target value of 0.8, ensuring that structural changes are limited  
708 to preserve key pharmacophore features:

709 
$$\mathcal{L}_{sim} = |sim_{start} - 0.8| \quad (18)$$

710 where  $Sim_{start}$  is the molecular encoding similarity between current encoding with start  
711 molecule. The second term is defined by

712 
$$\mathcal{L}_{prop} = \sum_{\{j \in J\}} |c_j - f_{prop_j}(\mathbf{E})| \quad (19)$$

713 where  $f_{prop}(\mathbf{E})$  represents the predicted molecular property, and  $c_j$  is the predefined target  
714 value for property  $j \in J$ . This formulation guides the optimization process while  
715 maintaining a balance between multiple objectives. In this study,  $J$  consists of three  
716 molecular properties: solubility, membrane permeability, and lipophilicity.

717 The total loss function is expressed as:

718 
$$\mathcal{L} = \frac{count(J)}{0.2} \times \mathcal{L}_{sim} + \mathcal{L}_{prop} \quad (20)$$

719 Besides optimizing molecular properties, directed migration can be used to migrate one  
720 molecular structure to another and to observe changes in molecular structure along the  
721 migration pathway within the encoding space constructed through representation learning.  
722 This method is applicable to scaffold hopping, which involves transitioning between  
723 molecular scaffolds, and to the fusion of scaffolds with two distinct properties. The loss  
724 function can be expressed as:

725 
$$\mathcal{L} = 1 - sim_{target} \quad (21)$$

726 where  $sim_{target}$  is the similarity between current encoding vector and the target molecular  
727 encoding.

728 In the practice of scaffold hopping, the molecules generated from the directed migration  
729 are docked into the PDE4B protein structures (PDB code: 4KP6<sup>63</sup> and 3O56<sup>64</sup>) using the  
730 Glide SP (Standard Precision)<sup>62</sup> docking tool to evaluate their docking scores. The docking  
731 pose is visualized by ChimeraX<sup>65</sup>.

732 **Chemical Fusion.** Chemical fusion is an alternative approach to molecular generation  
733 by combining structural elements from reference compounds. Similar to directed migration,  
734 chemical fusion also uses optimizers and loss functions. Starting from the initial molecular  
735 encoding vector (enumerated from reference molecules), the optimization is performed  
736 using the AdamW<sup>52</sup> optimizer with a learning rate  $3.0 \times 10^{-5}$  for 1,000 steps. After each

737 step, the encoding vector is converted into a molecular structure using a molecular structure  
738 decoder with a temperature of 0.4 (**Figure S13b**).

739 For reference molecules  $r \in R$  and current molecular encoding  $E$ , the similarity loss is  
740 denoted as:

741 
$$\mathcal{L} = \min_{\{r \in R\}} \left( \frac{1}{1 + 10000^{\text{sim}(E_r, E) - 0.6}} \right) \quad (22)$$

742 where the  $E_r$  is the molecular encoding of  $r$ .  $\mathcal{L}$  could be considered as the minimum  
743 distance between the current molecule and the reference molecule, and minimizing this  
744 distance could produce a fusion between the molecules.

745 In the practice of multi-target drug design, the molecules generated from the chemical  
746 fusion are docked into protein structures of AURKA (PDB ID: 5DT0<sup>66</sup>) and PI3K $\gamma$  (PDB  
747 ID: 3ML8<sup>67</sup>) using the Glide SP (Standard Precision)<sup>62</sup>. Subsequently, the Prime module in  
748 the Schrödinger software package was used to calculate the MM-GBSA binding free  
749 energy  $\Delta G_{MM-GBSA}$  between the docking pose and target protein, where amino acids within  
750 5 Å around the ligand are set as flexible regions and energy minimization is practiced.  
751 Finally, the ligand efficiency  $LE$  is calculated by:

752 
$$LE = \frac{\Delta G_{MM-GBSA}}{1 + \ln(N_{\text{heavy atoms}})} \quad (23)$$

753 where  $N_{\text{heavy atoms}}$  refers to number of non-hydrogen atoms.

754

## 755 Data availability

756 All molecular and benchmark datasets used in this study are collected from public  
757 resources and can be downloaded from <https://zhanglab.comp.nus.edu.sg/Ouroboros/> and  
758 <https://github.com/Wang-Lin-boop/Ouroboros>.

759

## 760 Code availability

761 Source codes and standalone package of the Ouroboros model are released under the  
762 MIT License and can be accessed at <https://zhanglab.comp.nus.edu.sg/Ouroboros/> and  
763 <https://github.com/Wang-Lin-boop/Ouroboros>.

764

## 765 Acknowledgements

766 We thank Shihang Wang, Bing Ye, Dr. Wei-kang Gong, Prof. Fang Bai, and Prof. Peng  
767 Zhan for their valuable help and insightful discussions. We also appreciate the support and  
768 services provided by ICE Bioscience Inc. in conducting the enzyme activity assays.  
769 Additionally, we are grateful to the BioHPC platform of the Institute of Systems Medicine,  
770 the Biomedical High-Performance Computing Platform of the Chinese Academy of  
771 Medical Sciences, and the Beijing Super Cloud Center for providing computational  
772 resources. This work was supported in part by the Singapore Ministry of Education (T1  
773 251RES2309) and the National University of Singapore Startup Grants (#A-8001129-00-  
774 00 and #A-0009651-30-00). L.W. acknowledges support from the Young Scholars Program  
775 of the Chinese Academy of Medical Sciences.

776

## 777 Author contributions

778 L.W. and Y.Z. conceived the project and designed the experiments; L.W. developed  
779 methods and designed and performed experiments; Y.W., H.L., M.L., Y.Z., C.C., C.L., and  
780 J.Z. helped with data collection and insightful discussion; L.W. wrote the initial manuscript;  
781 Y.Z. revised the manuscript; all authors proofread and approved the final manuscript.  
782

783 **Competing interests**

784 H.L., M.L., C.C., C.L. and J.Z are affiliated with DeepMed Technology (Suzhou) Co.,  
785 Ltd, but this affiliation did not influence the study design, data analysis, or interpretation  
786 of results. The authors declare no other competing interests.  
787

788 **References**

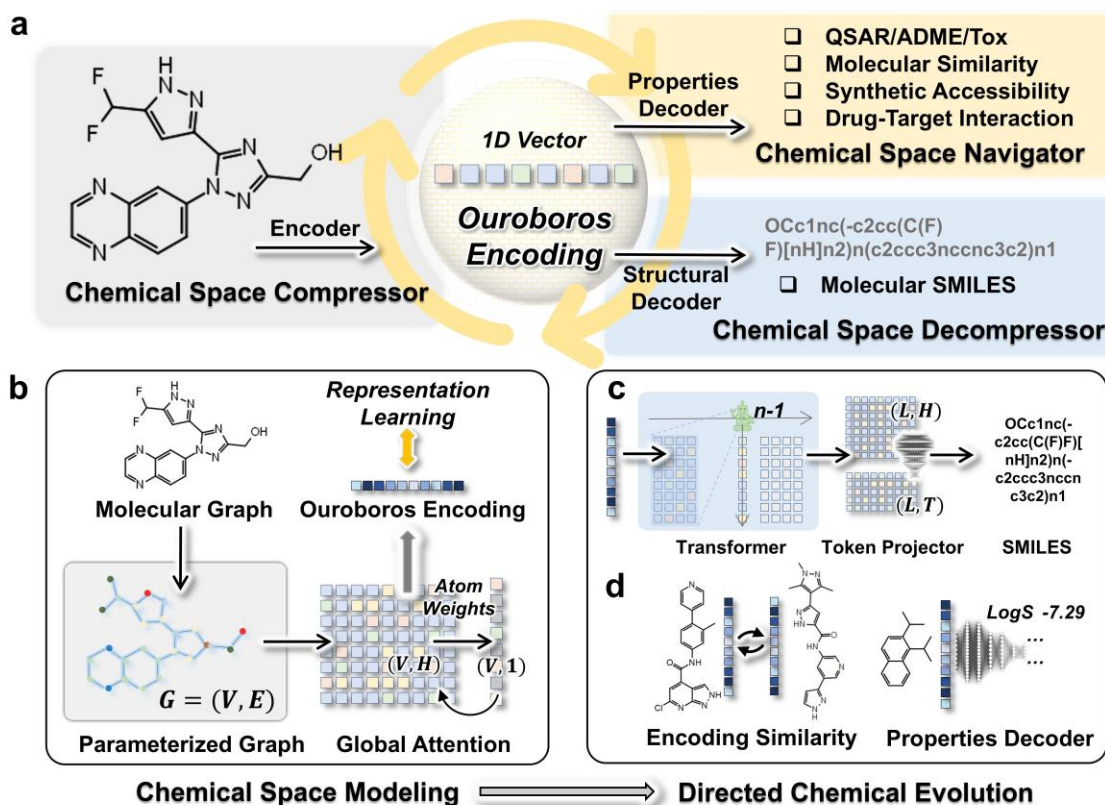
- 789 1. Rumelhart, D. E., Hinton, G. E. & Williams, R. J. Learning representations by back-  
790 propagating errors. *Nature* **323**, 533–536 (1986).
- 791 2. Lecun, Y., Bengio, Y. & Hinton, G. Deep learning. *Nature* **521**, 436–444 (2015).
- 792 3. Ouyang, L. *et al.* Training language models to follow instructions with human  
793 feedback. *Adv. Neural Inf. Process. Syst.* **35**, (2022).
- 794 4. Radford, A. *et al.* Learning Transferable Visual Models From Natural Language  
795 Supervision. *Proc. Mach. Learn. Res.* **139**, 8748–8763 (2021).
- 796 5. Ramesh, A., Dhariwal, P., Nichol, A., Chu, C. & Chen, M. Hierarchical Text-  
797 Conditional Image Generation with CLIP Latents. (2022).
- 798 6. Wigh, D. S., Goodman, J. M. & Lapkin, A. A. A review of molecular representation  
799 in the age of machine learning. *Wiley Interdiscip. Rev. Comput. Mol. Sci.* **12**, (2022).
- 800 7. Fang, X. *et al.* Geometry-enhanced molecular representation learning for property  
801 prediction. *Nat. Mach. Intell.* **4**, 127–134 (2022).
- 802 8. Zhou, G. *et al.* Uni-Mol: a Universal 3D Molecular Representation Learning  
803 Framework. *11th Int. Conf. Learn. Represent.* 1–20 (2023).
- 804 9. Wang, L. *et al.* Conformational Space Profiling Enhances Generic Molecular  
805 Representation for AI-Powered Ligand-Based Drug Discovery. *Adv. Sci.* (2024)  
806 doi:10.1002/advs.202403998.
- 807 10. Liu, S. *et al.* Pre-Training Molecular Graph Representation With 3D Geometry.  
808 *ICLR 2022 - 10th Int. Conf. Learn. Represent.* (2022).
- 809 11. Tong, X. *et al.* Deep representation learning of chemical-induced transcriptional  
810 profile for phenotype-based drug discovery. *Nat. Commun.* **15**, (2024).
- 811 12. Hansch, C. & Fujita, T.  $\rho$ - $\sigma$ - $\pi$  Analysis. A Method for the Correlation of Biological  
812 Activity and Chemical Structure. *J. Am. Chem. Soc.* **86**, 5710 (1964).
- 813 13. Tropsha, A., Isayev, O., Varnek, A., Schneider, G. & Cherkasov, A. Integrating  
814 QSAR modelling and deep learning in drug discovery: the emergence of deep QSAR.  
815 *Nat. Rev. Drug Discov.* **23**, 141–155 (2024).
- 816 14. Méndez-Lucio, O., Baillif, B., Clevert, D. A., Rouquié, D. & Wichard, J. De novo  
817 generation of hit-like molecules from gene expression signatures using artificial  
818 intelligence. *Nat. Commun.* **11**, (2020).
- 819 15. Abeer, A. N. M. N., Urban, N. M., Weil, M. R., Alexander, F. J. & Yoon, B.-J.  
820 Multi-objective latent space optimization of generative molecular design models.  
821 *Patterns* 101042 (2024) doi:10.1016/j.patter.2024.101042.
- 822 16. Born, J. & Manica, M. Regression Transformer enables concurrent sequence  
823 regression and generation for molecular language modelling. *Nat. Mach. Intell.* **5**,

- 824 432–444 (2023).
- 825 17. Zhang, O. *et al.* ResGen is a pocket-aware 3D molecular generation model based on  
826 parallel multiscale modelling. *Nat. Mach. Intell.* **5**, 1020–1030 (2023).
- 827 18. Huang, L. *et al.* A dual diffusion model enables 3D molecule generation and lead  
828 optimization based on target pockets. *Nat. Commun.* **15**, (2024).
- 829 19. Tibo, A., He, J., Janet, J. P., Nittinger, E. & Engkvist, O. Exhaustive local chemical  
830 space exploration using a transformer model. *Nat. Commun.* **15**, (2024).
- 831 20. Li, Y., Zemel, R., Brockschmidt, M. & Tarlow, D. Gated graph sequence neural  
832 networks. *4th Int. Conf. Learn. Represent. ICLR 2016 - Conf. Track Proc.* (2016).
- 833 21. Mysinger, M. M., Carchia, M., Irwin, J. J. & Shoichet, B. K. Directory of useful  
834 decoys, enhanced (DUD-E): Better ligands and decoys for better benchmarking. *J.  
835 Med. Chem.* **55**, 6582–6594 (2012).
- 836 22. Tran-Nguyen, V. K., Jacquemard, C. & Rognan, D. LIT-PCBA: An unbiased data  
837 set for machine learning and virtual screening. *J. Chem. Inf. Model.* **60**, 4263–4273  
838 (2020).
- 839 23. Truchon, J. F. & Bayly, C. I. Evaluating virtual screening methods: Good and bad  
840 metrics for the ‘early recognition’ problem. *J. Chem. Inf. Model.* **47**, 488–508 (2007).
- 841 24. Cai, H., Zhang, H., Zhao, D., Wu, J. & Wang, L. FP-GNN: a versatile deep learning  
842 architecture for enhanced molecular property prediction. *Brief. Bioinform.* **23**,  
843 (2022).
- 844 25. Kanakala, G. C., Devata, S., Chatterjee, P. & Priyakumar, U. D. Generative artificial  
845 intelligence for small molecule drug design. *Curr. Opin. Biotechnol.* **89**, (2024).
- 846 26. Chithrananda, S., Grand, G. & Ramsundar, B. ChemBERTa: Large-Scale Self-  
847 Supervised Pretraining for Molecular Property Prediction. *arXiv* (2020).
- 848 27. Ahmad, W., Simon, E., Chithrananda, S., Grand, G. & Ramsundar, B. ChemBERTa-  
849 2: Towards Chemical Foundation Models. (2022).
- 850 28. Smith, D. H., Carhart, R. E. & Venkataraghavan, R. Atom Pairs as Molecular  
851 Features in Structure-Activity Studies: Definition and Applications. *J. Chem. Inf.  
852 Comput. Sci.* **25**, 64–73 (1985).
- 853 29. Huijben, I. A. M., Kool, W., Paulus, M. B. & Van Sloun, R. J. G. A Review of the  
854 Gumbel-max Trick and its Extensions for Discrete Stochasticity in Machine  
855 Learning. *IEEE Trans. Pattern Anal. Mach. Intell.* **45**, 1353–1371 (2023).
- 856 30. Agarap, A. F. Deep Learning using Rectified Linear Units (ReLU). *arXiv* (2018).
- 857 31. Jin, W., Coley, C. W., Barzilay, R. & Jaakkola, T. Predicting organic reaction  
858 outcomes with weisfeiler-lehman network. *Adv. Neural Inf. Process. Syst.* **2017-Decem**,  
859 2608–2617 (2017).
- 860 32. Li, M. *et al.* DGL-LifeSci: An Open-Source Toolkit for Deep Learning on Graphs  
861 in Life Science. *ACS Omega* **6**, 27233–27238 (2021).
- 862 33. Wang, M. *et al.* Deep Graph Library: A Graph-Centric, Highly-Performant Package  
863 for Graph Neural Networks. *arXiv* (2019).
- 864 34. Wang, S. *et al.* PhenoScreen: A Dual-Space Contrastive Learning Framework-based  
865 Phenotypic Screening Method by Linking Chemical Perturbations to Cellular  
866 Morphology. *bioRxiv* (2024) doi:10.1101/2024.10.23.619752.
- 867 35. Maas, A. L., Hannun, A. Y. & Ng, A. Y. Rectifier nonlinearities improve neural  
868 network acoustic models. *ICML Work. Deep Learn. Audio, Speech Lang. Process.*  
869 (2013).

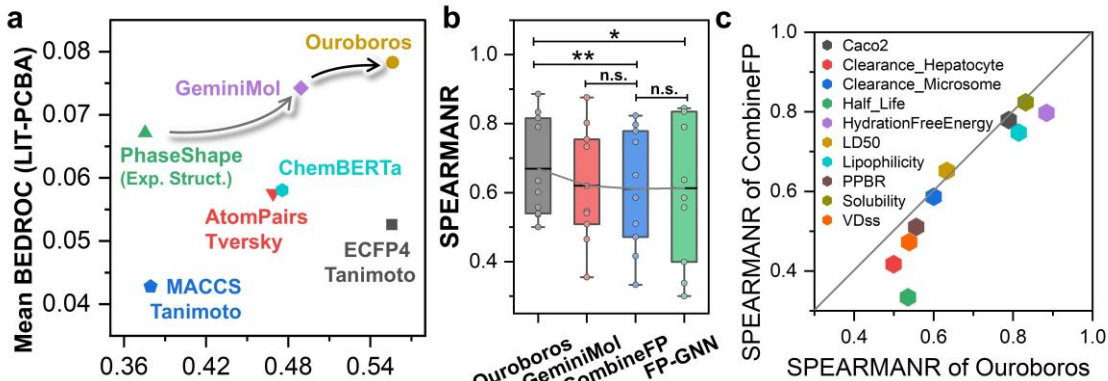
- 870 36. Elfwing, S., Uchibe, E. & Doya, K. Sigmoid-weighted linear units for neural  
871 network function approximation in reinforcement learning. *Neural Networks* **107**,  
872 3–11 (2018).
- 873 37. Agostinelli, F., Hoffman, M., Sadowski, P. & Baldi, P. Learning activation functions  
874 to improve deep neural networks. *3rd Int. Conf. Learn. Represent. ICLR 2015 -*  
875 *Work. Track Proc.* 1–9 (2015).
- 876 38. Bostrom, K. & Durrett, G. Byte pair encoding is suboptimal for language model  
877 pretraining. *Find. Assoc. Comput. Linguist. Find. ACL EMNLP 2020* 4617–4624  
878 (2020) doi:10.18653/v1/2020.findings-emnlp.414.
- 879 39. Vaswani, A. *et al.* Attention is all you need. *Adv. Neural Inf. Process. Syst.* **2017-Decem**, 5999–6009 (2017).
- 880 40. Li, J. *et al.* CycPeptMPDB: A Comprehensive Database of Membrane Permeability  
881 of Cyclic Peptides. *J. Chem. Inf. Model.* **63**, 2240–2250 (2023).
- 882 41. Wauer, M. J. *et al.* Toward performance-diverse small-molecule libraries for cell-  
883 based phenotypic screening using multiplexed high-dimensional profiling. *Proc.  
884 Natl. Acad. Sci. U. S. A.* **111**, 10911–10916 (2014).
- 885 42. Huang, J. *et al.* A dataset of images and morphological profiles of 30 000 small-  
886 molecule treatments using the Cell Painting assay. *Gigascience* **6**, 1 (2017).
- 887 43. Berman, H. M. *et al.* The Protein Data Bank. *Nucleic Acids Res.* **28**, 235–242 (2000).
- 888 44. Johnston, R. C. *et al.* Epik: pKa and Protonation State Prediction through Machine  
889 Learning. *J. Chem. Theory Comput.* **19**, 2380–2388 (2023).
- 890 45. Sastry, G. M., Dixon, S. L. & Sherman, W. Rapid shape-based ligand alignment and  
891 virtual screening method based on atom/feature-pair similarities and volume overlap  
892 scoring. *J. Chem. Inf. Model.* **51**, 2455–2466 (2011).
- 893 46. Chang, G., Guida, W. C. & Still, W. C. An Internal Coordinate Monte Carlo Method  
894 for Searching Conformational Space. *J. Am. Chem. Soc.* **111**, 4379–4386 (1989).
- 895 47. Mohamadi, F. *et al.* Macromodel—an integrated software system for modeling  
896 organic and bioorganic molecules using molecular mechanics. *J. Comput. Chem.* **11**,  
897 440–467 (1990).
- 898 48. Watts, K. S., Dalal, P., Tebben, A. J., Cheney, D. L. & Shelley, J. C. Macrocycle  
899 conformational sampling with macromodel. *J. Chem. Inf. Model.* **54**, 2680–2696  
900 (2014).
- 901 49. Lu, C. *et al.* OPLS4: Improving force field accuracy on challenging regimes of  
902 chemical space. *J. Chem. Theory Comput.* **17**, 4291–4300 (2021).
- 903 50. Rogers, D. & Hahn, M. Extended-connectivity fingerprints. *J. Chem. Inf. Model.* **50**,  
904 742–754 (2010).
- 905 51. Bath, P. A., Morris, C. A. & Willett, P. Effect of standardization on fragment-based  
906 measures of structural similarity. *J. Chemom.* **7**, 543–550 (1993).
- 907 52. Loshchilov, I. & Hutter, F. Decoupled weight decay regularization. *7th Int. Conf.  
908 Learn. Represent. ICLR 2019* (2019).
- 909 53. Paszke, A. *et al.* PyTorch: An imperative style, high-performance deep learning  
910 library. *Adv. Neural Inf. Process. Syst.* **32**, (2019).
- 911 54. Sun, Y. *et al.* A Length-Extrapolatable Transformer. *Proc. Annu. Meet. Assoc.  
912 Comput. Linguist.* **1**, 14590–14604 (2023).
- 913 55. Su, J. *et al.* RoFormer: Enhanced Transformer with Rotary Position Embedding.  
914 *Neurocomputing* **568**, (2021).
- 915

- 916 56. Huang, K. *et al.* Therapeutics Data Commons: Machine Learning Datasets and  
917 Tasks for Drug Discovery and Development. *arXiv* (2021).
- 918 57. Nilakantan, R., Bauman, N., Venkataraghavan, R. & Dixon, J. S. Topological  
919 Torsion: A New Molecular Descriptor for SAR Applications. Comparison with  
920 Other Descriptors. *J. Chem. Inf. Comput. Sci.* **27**, 82–85 (1987).
- 921 58. Greg Landrum. RDKit: Open-source cheminformatics. at  
922 <https://doi.org/10.5281/zenodo.8254217> (2010).
- 923 59. Shi, X. Multimodal AutoML on Tables with Text Fields. *8th ICML Work. Autom.*  
924 *Mach. Learn.* **1**, 1–15 (2021).
- 925 60. Ke, G. *et al.* LightGBM: A highly efficient gradient boosting decision tree. *Adv.*  
926 *Neural Inf. Process. Syst.* **2017-Decem**, 3147–3155 (2017).
- 927 61. Prokhorenkova, L., Gusev, G., Vorobev, A., Dorogush, A. V. & Gulin, A. Catboost:  
928 Unbiased boosting with categorical features. *Adv. Neural Inf. Process. Syst.* **2018-**  
929 **Decem**, 6638–6648 (2018).
- 930 62. Halgren, T. A. *et al.* Glide: A New Approach for Rapid, Accurate Docking and  
931 Scoring. 2. Enrichment Factors in Database Screening. *J. Med. Chem.* **47**, 1750–  
932 1759 (2004).
- 933 63. Gewald, R., Grunwald, C. & Egerland, U. Discovery of triazines as potent, selective  
934 and orally active PDE4 inhibitors. *Bioorganic Med. Chem. Lett.* **23**, 4308–4314  
935 (2013).
- 936 64. Mitchell, C. J. *et al.* Pyrazolopyridines as potent PDE4B inhibitors: 5-Heterocycle  
937 SAR. *Bioorganic Med. Chem. Lett.* **20**, 5803–5806 (2010).
- 938 65. Pettersen, E. F. *et al.* UCSF ChimeraX: Structure visualization for researchers,  
939 educators, and developers. *Protein Sci.* **30**, 70–82 (2021).
- 940 66. Janeček, M. *et al.* Allosteric modulation of AURKA kinase activity by a small-  
941 molecule inhibitor of its protein-protein interaction with TPX2. *Sci. Rep.* **6**, (2016).
- 942 67. Cheng, H. *et al.* Discovery of the highly potent PI3K/mTOR dual inhibitor PF-  
943 04979064 through structure-based drug design. *ACS Med. Chem. Lett.* **4**, 91–97  
944 (2013).
- 945
- 946
- 947

948 **Figures**  
949

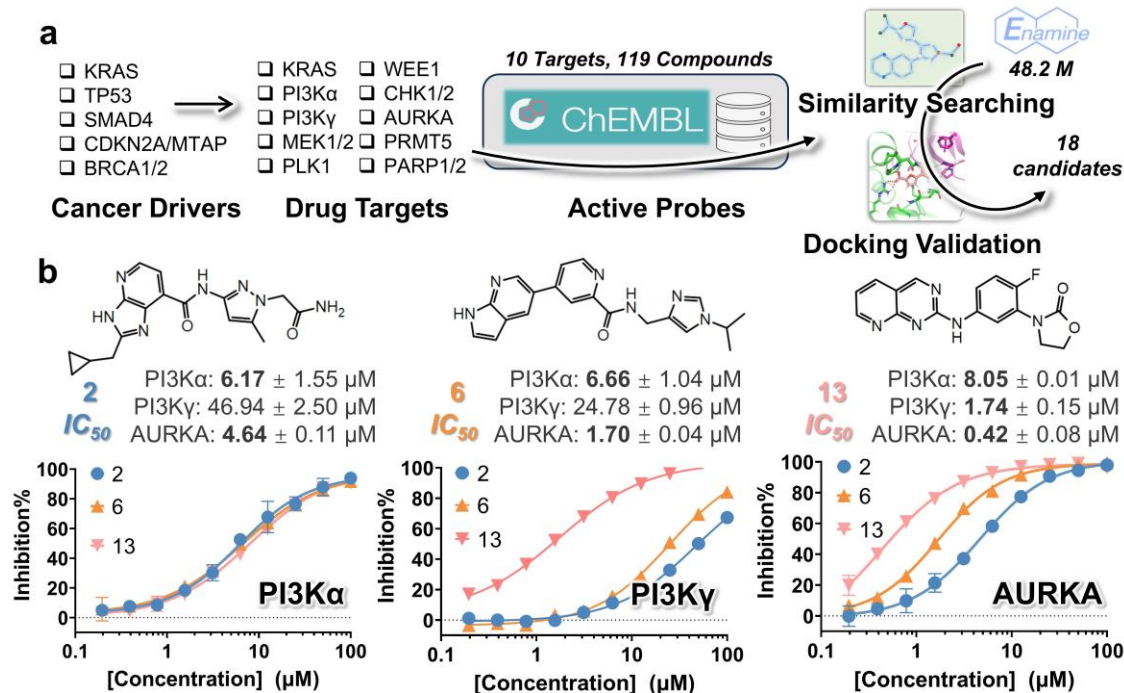


950  
951 **Figure 1 | The Ouroboros protocol for chemical space navigation.** (a) Three independent  
952 modules of Ouroboros. The chemical space compressor converts molecular graphs into 1D vectors,  
953 typically implemented by a graph neural network (GNN), while the property decoder projects the  
954 1D vectors onto molecular properties through a multilayer perceptron (MLP). Finally, the chemical  
955 space decompressor transforms these 1D vectors into SMILES representations, utilizing a text  
956 generation model by Transformer decoder. (b) The molecular encoder for chemical space modeling,  
957 where the molecular graph is encoded by a global-attention based GNN module and represented as  
958 a 1D encoded vector, with ‘E’ referring to bonds, ‘V’ to atoms, and “H” to hidden size. (c) The  
959 molecular decoder for decompressing the molecular encoding to molecular structure, with ‘L’ refer  
960 to sequence length. (d) The two approachs for chemical space navigations.  
961



962  
963  
964  
965  
966  
967  
968  
969  
970  
971  
972  
973  
974  
975  
976

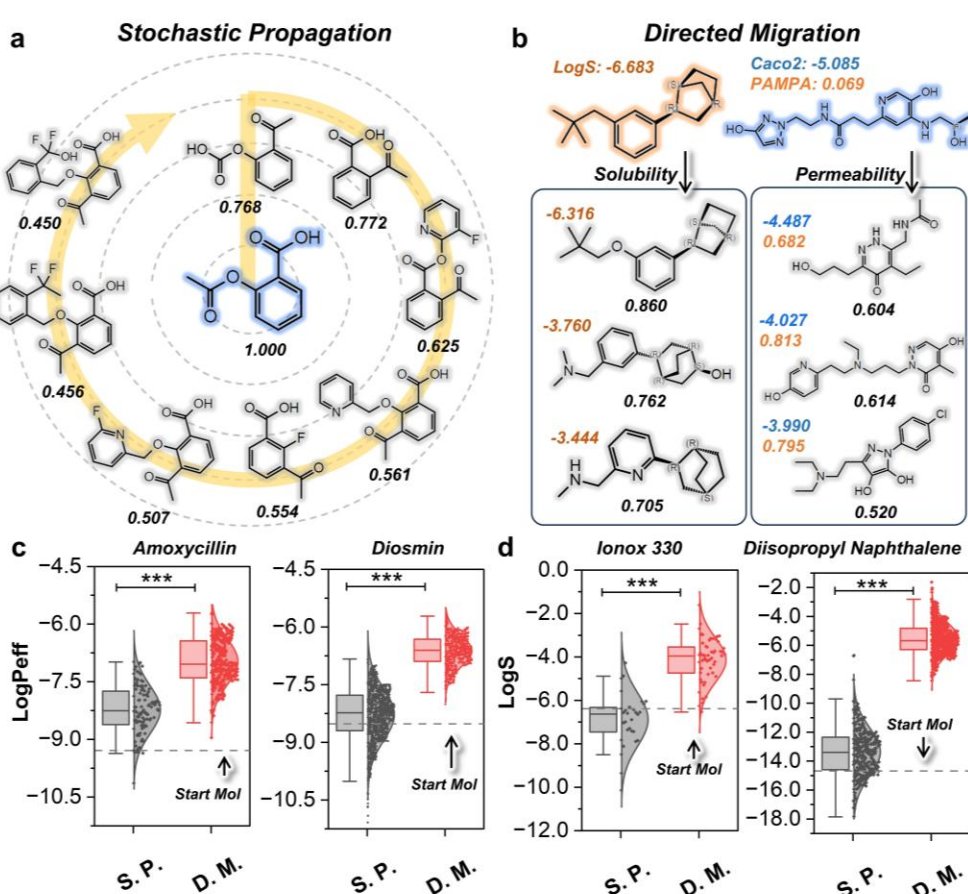
**Figure 2 | Assessing the quality of chemical space modeling in Ouroboros.** (a) Similarity-based virtual screening performance evaluated by the mean BEDROC on the 102 targets from DUD-E versus that on the 15 targets from LIT-PCBA by different methods, including Ouroboros, GeminiMol, PhaseShape, ChemBERTa (the best performend version of ChemMLM), AtomPairs, ECFP4, and MACCS. (b) Spearman correlation coefficients achieved by three molecular encoders on 10 different molecular property regression tasks. For GeminiMol and Ouroboros, the decoder is constructed using a multilayer perceptron. CombineFP combines four molecular fingerprints together, including AtomPairs, TopologicalTorsion, ECFP4, and FCFP6, which uses AutoGluon to construct property predictors. ‘\*\*’ refers to p-value=0.0079, ‘\*’ to p-value=0.0540, and ‘n.s.’ to not significant (p-value>0.3). (c) Spearman correlation coefficients by Ouroboros on 10 different molecular property regression tasks (colored differently) versus that by CombineFP.



977  
978  
979  
980  
981  
982  
983

**Figure 3 | The discovery of novel multi-target inhibitors using Ouroboros. (a)** A pipeline for screening potential multi-target cancer driver inhibitors. **(b)**  $IC_{50}$  and inhibition curves of three hit compounds (#2, #6 and #13) for three targets, including PI3K $\alpha$ , PI3K $\gamma$  and AURKA.

984

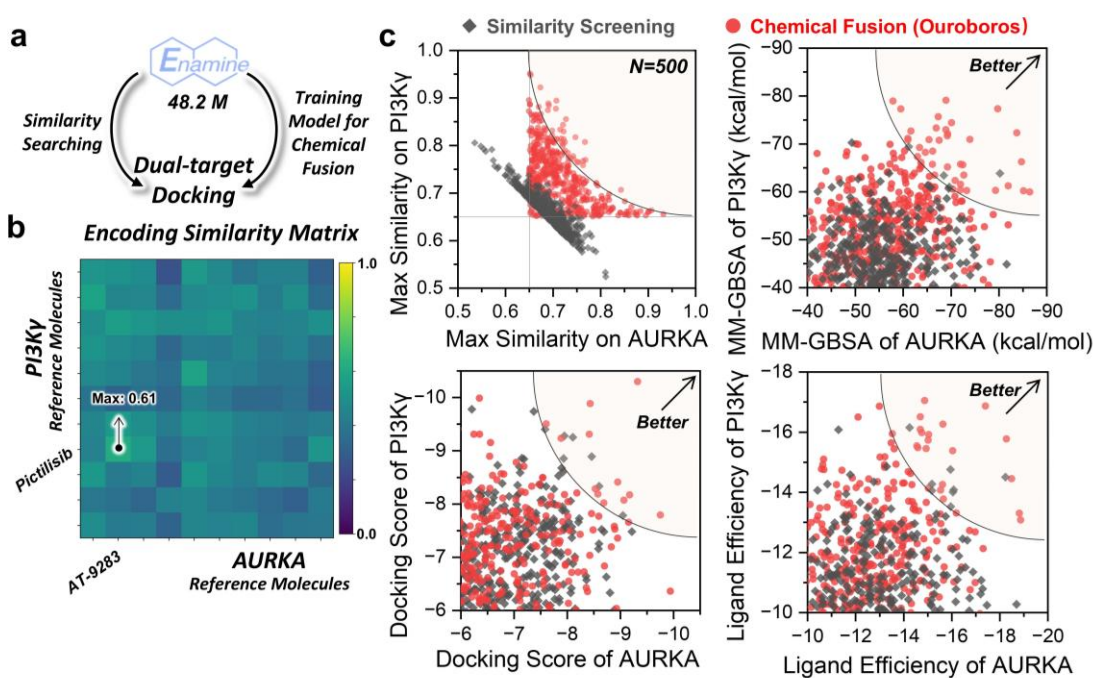


985

**Figure 4 | Exploring chemical space with Ouroboros.** (a) Stochastic propagation from aspirin. Encoding similarities with start molecule are marked at the bottom of molecules. (b) Directed migration for optimizing solubility and membrane permeability. The property labels are predictions from the property predictor trained during the benchmark test. The encoding similarity values are displayed beneath each molecule. Solubility is represented by LogS (shown in brown, positioned to the left of each molecule), while membrane permeability is indicated by LogPeff (measured in  $10^{-6}$  cm/s). Parallel artificial membrane permeability values are highlighted in orange, and Caco-2 cell permeability values are shown in blue. PAMPA (Parallel Artificial Membrane Permeability Assay) is also included as a reference. (c, d) The comparison of stochastic propagation (S.P.) and directed migration (D.M.) in multi-objective molecular properties optimization for membrane permeability (c) and solubility (d). The dashed line represents the starting molecule. All the points in the box plots represent new molecules with encoding similarity greater than 0.6 generated during the propagation process and migration pathway. “\*\*\*” refers to  $p\text{-value} < 0.0001$ .

999

1000



1001

**Figure 5 | The chemical fusions in encoding space for dual-target drug discovery.** (a) Comparison of similarity-based virtual screening and Ouroboros chemical evolution. (b) The encoding similarity matrix between reference molecules of AURKA and PI3K $\gamma$ . The pair of molecules with the highest similarity is pointed out with arrows. (c) Assessment of molecules generated using chemical fusion and similarity screening. The black diamonds represent molecules produced by similarity screening, and the red circles represent molecules produced by chemical fusion. A solid gray line in the figure represents the similarity threshold of 0.65 that was used to filter the molecules produced in the chemical fusion. The translucent sectors in the upper right corner represent high-quality candidate molecules.

1002

1003

1004

1005

1006

1007

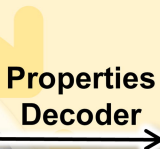
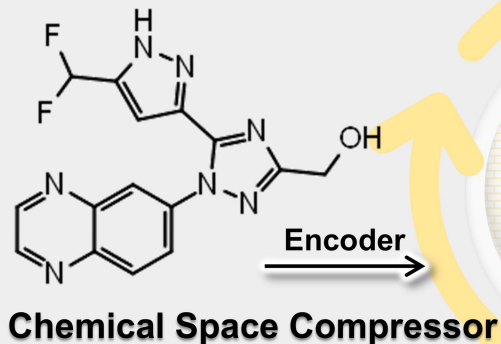
1008

1009

1010

1011

1012

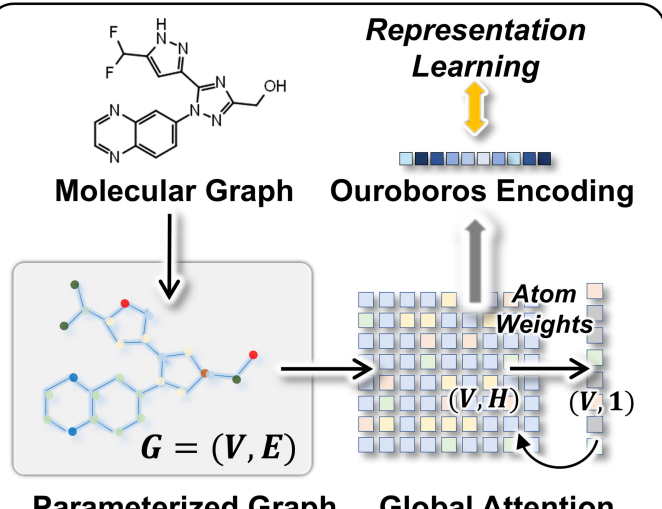
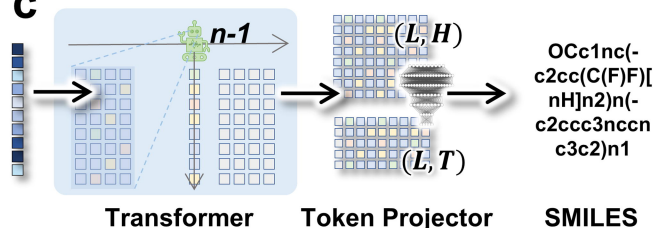
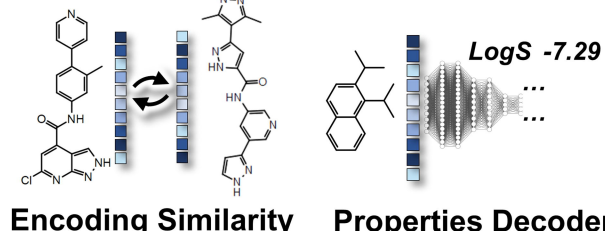
**a**

- QSAR/ADME/Tox
  - Molecular Similarity
  - Synthetic Accessibility
  - Drug-Target Interaction
- Chemical Space Navigator**

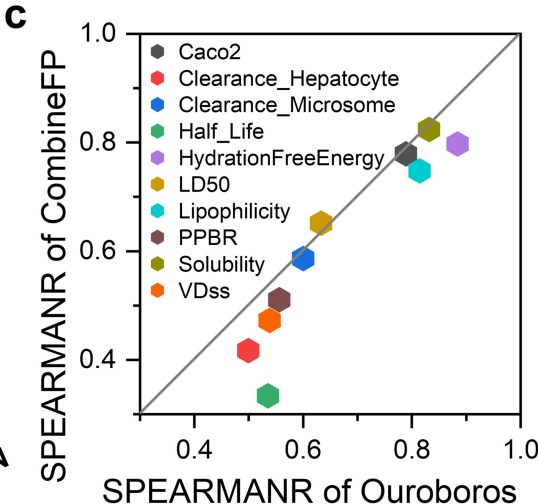
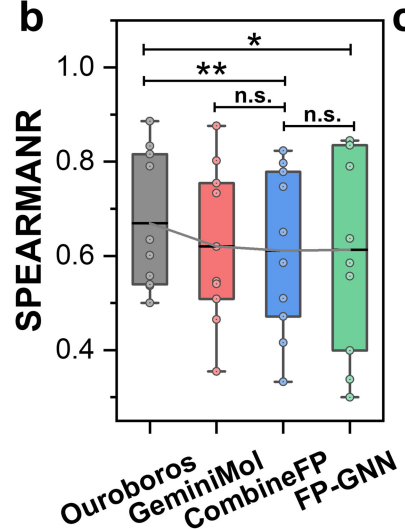
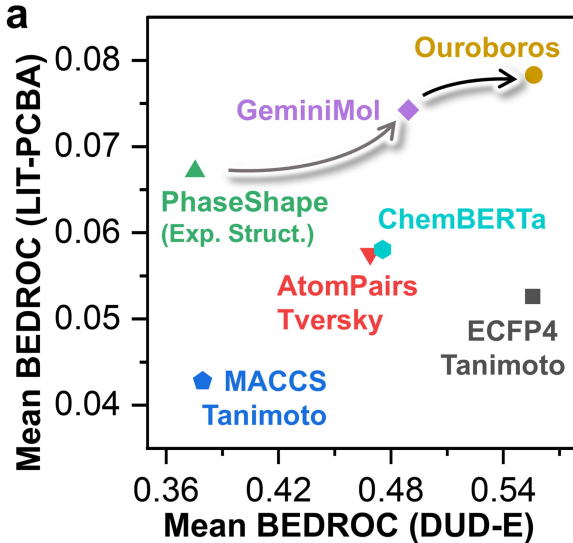
Oc1nc(-c2cc(C(F)F)[nH]n2)n(c2ccc3nccnc3c2)n1

- Molecular SMILES

**Chemical Space Decompressor**

**b****c****d**

**Chemical Space Modeling** → **Directed Chemical Evolution**



a

- KRAS
  - TP53
  - SMAD4
  - CDKN2A/MTAP
  - BRCA1/2

- KRAS
- PI3K $\alpha$
- PI3K $\gamma$
- MEK1/2
- PLK1
- WEE1
- CHK1/2
- AURKA
- PRMT5
- PARP1/2

## **10 Targets, 119 Compounds**



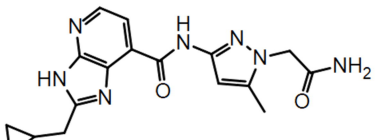
# Similarity Searching

## Cancer Drivers

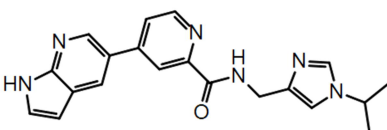
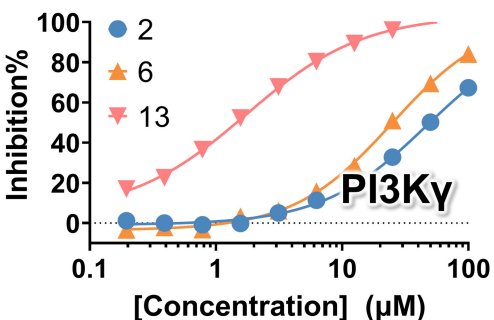
## Drug Targets

## Active Probes

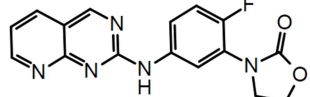
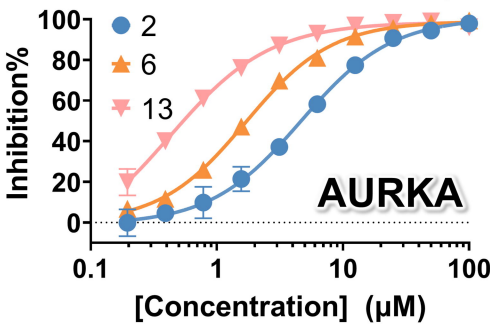
b



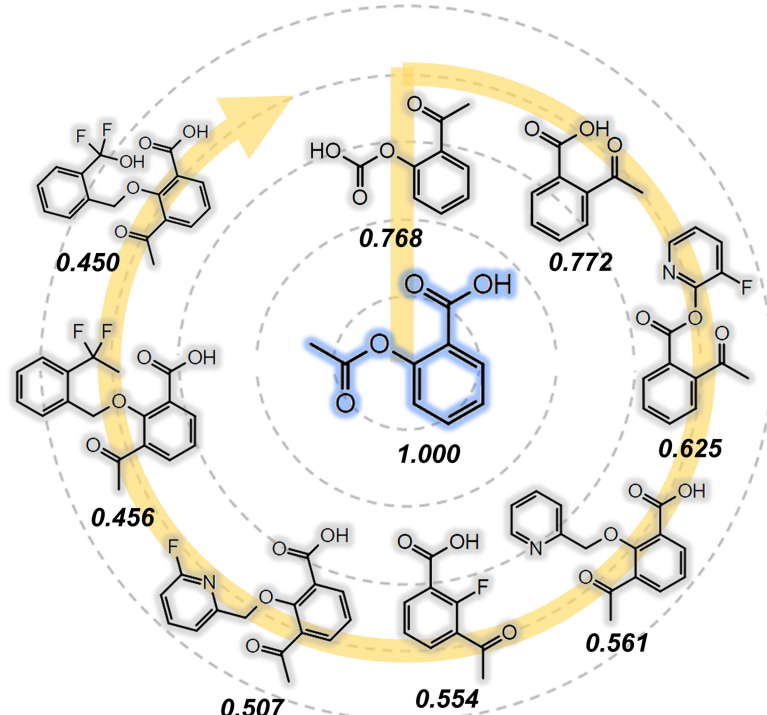
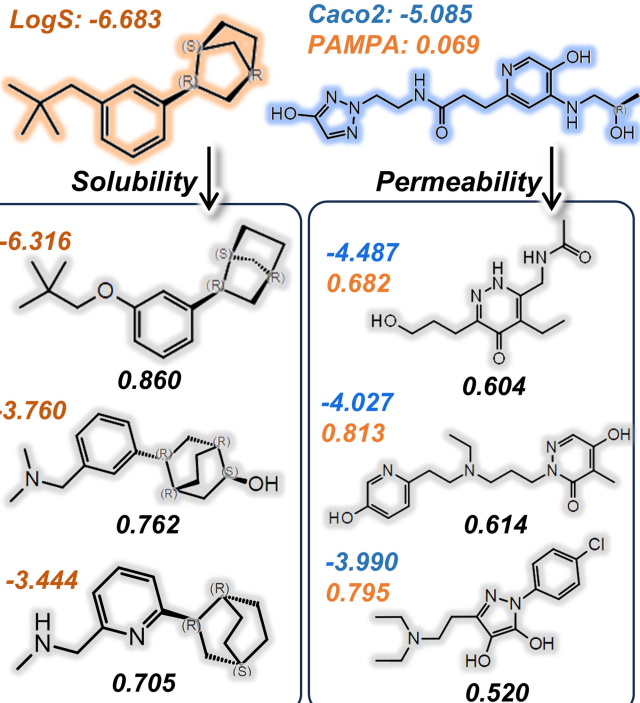
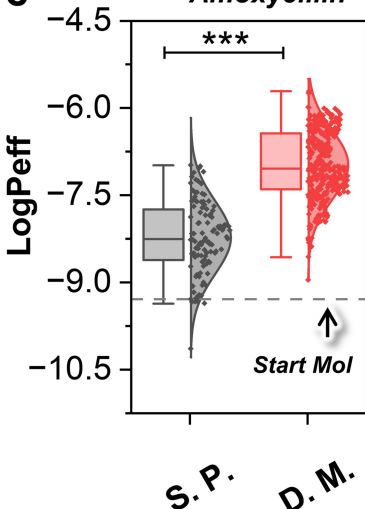
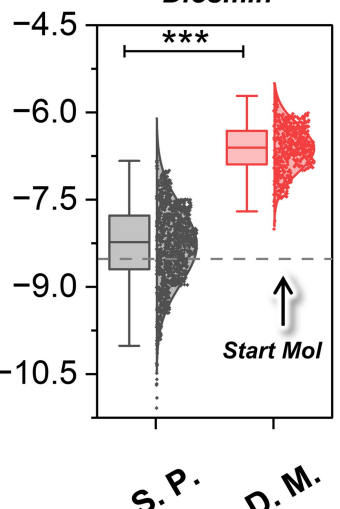
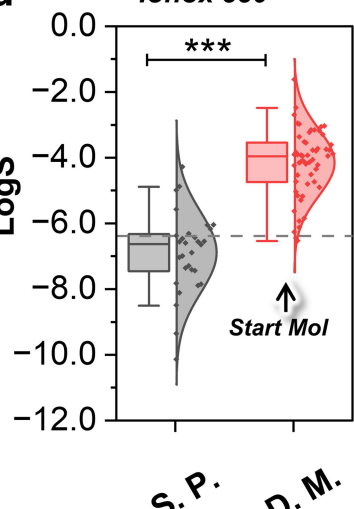
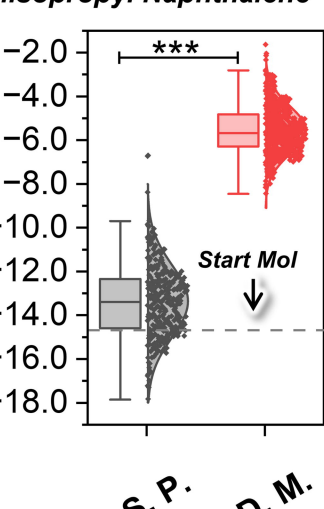
**2**  
**IC<sub>50</sub>** PI3Ka: 6.17 ± 1.55 µM  
PI3Ky: 46.94 ± 2.50 µM  
AURKA: 4.64 ± 0.11 µM

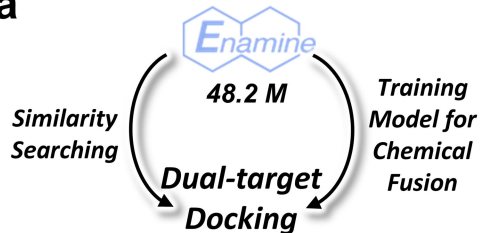


**6**  
**IC<sub>50</sub>** PI3K $\alpha$ : **6.66**  $\pm$  1.04  $\mu\text{M}$   
PI3K $\gamma$ : 24.78  $\pm$  0.96  $\mu\text{M}$   
AURKA: **1.70**  $\pm$  0.04  $\mu\text{M}$



PI3K $\alpha$ : **8.05**  $\pm$  0.01  $\mu$ M  
PI3K $\gamma$ : **1.74**  $\pm$  0.15  $\mu$ M  
AURKA: **0.42**  $\pm$  0.08  $\mu$ M

**a****Stochastic Propagation****b****Directed Migration****c****Amoxycillin****Diosmin****d****Ionoxy 330****Diisopropyl Naphthalene**

**a****b**